nature nanotechnology

Article

https://doi.org/10.1038/s41565-023-01545-6

3D spatiotemporally scalable in vivo neural probes based on fluorinated elastomers

Received: 3 May 2022

Accepted: 16 October 2023

Published online: 22 December 2023

Check for updates

Paul Le Floch[1,2,7], Siyuan Zhao[1,7], Ren Liu[1,7], Nicola Molinari[1], Eder Medina[1], Hao Shen[1], Zheliang Wang[3], Junsoo Kim[1], Hao Sheng[1], Sebastian Partarrieu[1], Wenbo Wang[1], Chanan Sessler[4,5], Guogao Zhang[1], Hyunsu Park[2], Xian Gong[2], Andrew Spencer[2], Jongha Lee[2], Tianyang Ye[2], Xin Tang[1], Xiao Wang[4,5], Katia Bertoldi[1], Nanshu Lu[3], Boris Kozinsky[1,6], Zhigang Suo[1] & Jia Liu[1]

Electronic devices for recording neural activity in the nervous system need to be scalable across large spatial and temporal scales while also providing millisecond and single-cell spatiotemporal resolution. However, existing high-resolution neural recording devices cannot achieve simultaneous scalability on both spatial and temporal levels due to a trade-off between sensor density and mechanical flexibility. Here we introduce a three-dimensional (3D) stacking implantable electronic platform, based on perfluorinated dielectric elastomers and tissue-level soft multilayer electrodes, that enables spatiotemporally scalable single-cell neural electrophysiology in the nervous system. Our elastomers exhibit stable dielectric performance for over a year in physiological solutions and are 10,000 times softer than conventional plastic dielectrics. By leveraging these unique characteristics we develop the packaging of lithographed nanometre-thick electrode arrays in a 3D configuration with a cross-sectional density of 7.6 electrodes per 100 μm^2. The resulting 3D integrated multilayer soft electrode array retains tissue-level flexibility, reducing chronic immune responses in mouse neural tissues, and demonstrates the ability to reliably track electrical activity in the mouse brain or spinal cord over months without disrupting animal behaviour.

Mapping the long-term stable activity of the central nervous system is important for neuroscience[1,2], addressing neurological disorders[3–5] and developing high-bandwidth brain–machine interfaces for neuroprosthetics and communications[6,7]. However, mapping neural activity is challenging as the functions of the central nervous system not only occur across multiple regions and depths of the tissue over months and years but also involve electrical activities that need to be quantified on the millisecond and micrometre scales of individual neurons. Among current technologies, implantable microelectrode arrays can simultaneously measure extracellular action potentials of thousands of single neurons at the millisecond timescale[6,8]. The number of electrodes can be increased further through three-dimensional (3D) stacking[9] or the integration of CMOS (complementary metal–oxide–semiconductor) multiplexing circuits[8]. However, their temporal scalability for the long-term stable recording of electrical activities from the same neurons is limited

[1]John A. Paulson School of Engineering and Applied Sciences, Harvard University, Boston, MA, USA. [2]Axoft, Inc., Cambridge, MA, USA. [3]Department of Aerospace Engineering and Engineering Mechanics, The University of Texas at Austin, Austin, TX, USA. [4]Broad Institute of MIT and Harvard, Cambridge, MA, USA. [5]Department of Chemistry, Massachusetts Institute of Technology, Cambridge, MA, USA. [6]Robert Bosch LLC Research and Technology Center, Watertown, MA, USA. [7]These authors contributed equally: Paul Le Floch, Siyuan Zhao, Ren Liu. e-mail: jia_liu@seas.harvard.edu

https://doi.org/10.1038/s41565-023-01545-6

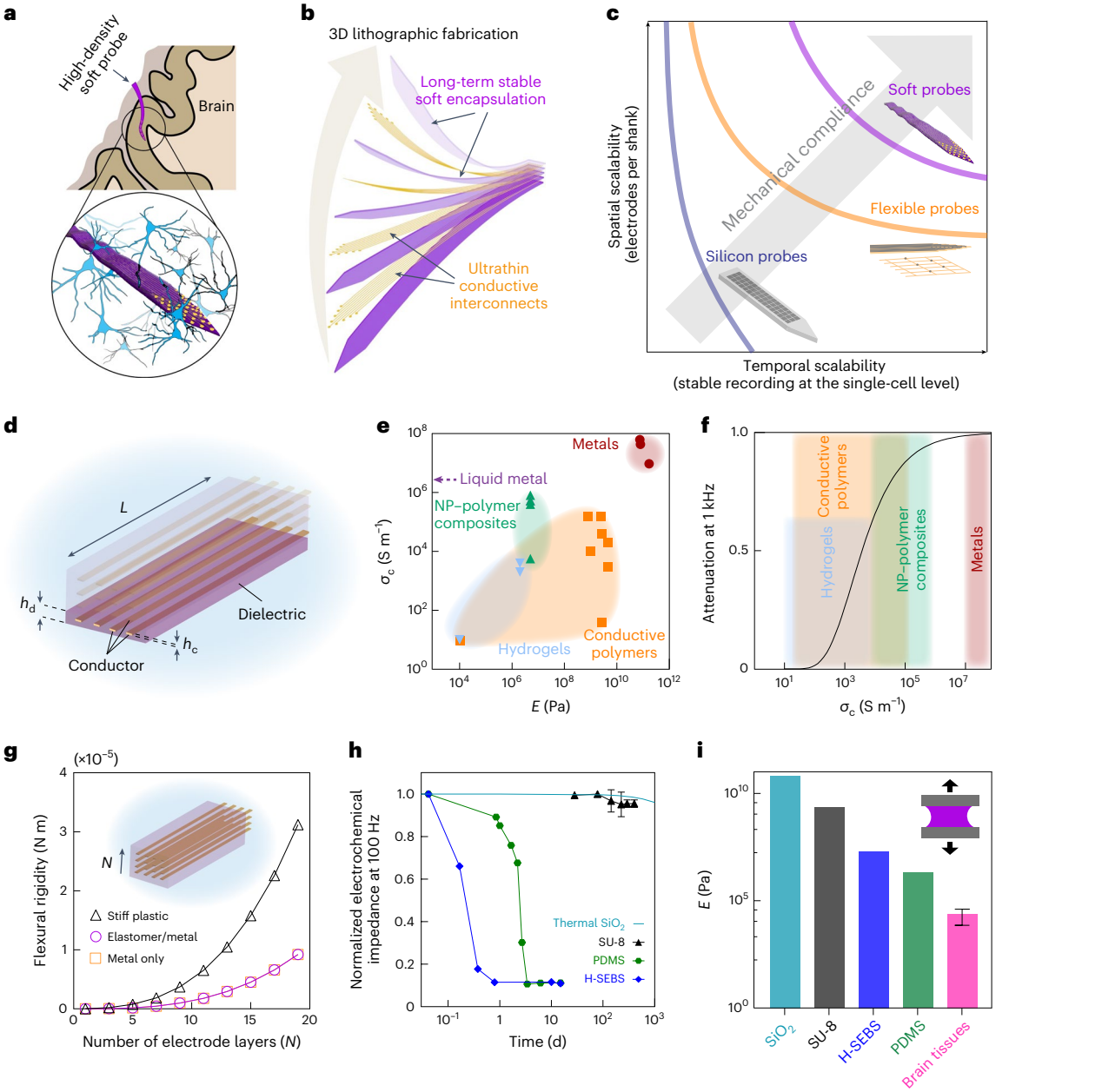

Fig. 1 | Implantable neural probes for spatiotemporally scalable in vivo electrophysiology. a, Schematic showing a spatiotemporally scalable neural probe implanted in the brain. The inset shows a 3D stacked microelectrode array encapsulated by soft elastomer layers, which can prevent ion permeation from the biofluid and maintain cell- and tissue-level mechanical properties, capable of providing a long-term stable interface with neurons at the single-cell level. **b**, Schematic illustrating the 3D lithographic fabrication of multilayer thin-film soft encapsulation/conductive interconnects to scale up the number of electrodes integrated on the neural probe. **c**, Spatial and temporal scalability of neural probes. Rigid silicon electronics can achieve high-density electrodes for neural recording but cannot stably record electrical activities from the same neurons over a long time period. Tissue-like flexible electronics can record electrical activities from the same neurons over a long time but do not offer scalability to increase the density and number of electrodes for neural recording. Soft electronics with a 3D electrode array can provide both spatial and temporal scalability for neural recording. **d**, Representative geometry of one layer of electrodes from a 3D stacked electrode array as a scalable neural probe, where L denotes the length of the interconnects, h_c denotes the thickness of the interconnects and h_d denotes the thickness of dielectric encapsulation. **e**, Conductivity of materials (σ_c) for flexible and soft electronics as a function of their elastic modulus (E)[26–36]. NP, nanoparticle. **f**, Attenuation of the voltage along an interconnect described in **d** as a function of the electrical conductivity of the materials. Parameters for simulation: $L = 2$ cm, $h_c = 40$ nm, $h_d = 1$ μm and $\varepsilon_d = 3.2$ for the dielectric constant of the encapsulation. **g**, Flexural rigidity of the neural probe as a function of the number of layers (N) of 3D integrated interconnects. Modulus values of 79 GPa, 4 GPa and 0.5 MPa are used for the simulation of metal interconnects, and plastic and elastomer encapsulations. Inset: schematic of a neural probe with $N = 4$ interconnects layers stacked vertically. **h**, Normalized electrochemical impedance of representative dielectric thin films as a function of the soaking time in 1x phosphate-buffered saline (PBS) solution at 37 °C. The SU-8 (an epoxy-based photoresist), polydimethylsiloxane (PDMS) and hydrogenated styrene-ethylene-butylene-styrene (H-SEBS) films have respective average thicknesses of 0.84 μm, 8.04 μm and 3.60 μm. For SU-8, the values are shown as the mean ± s.d. ($n = 4$ samples), and the PDMS and H-SEBS data are from our previous work[37]. For thermal silica (SiO_2), the model used is based on the etching rate measured in ref. 25. **i**, Elastic modulus values of dielectric materials compared with brain tissues[64]. Inset: schematic of the sample under uniaxial tension.

by probe drifting, chronic tissue damage and immune responses due to the large mechanical and structural disparities between the implantable electrodes and brain tissues[10].

The recent development of flexible thin-film nanoelectronics[6,11–15] tackles this issue by introducing biomimetic designs such as mesh nanoelectronics[12,16] and ultraflexible probes[6,13]. These designs reduce the thickness of stiff electronic structures to the submicrometre range, which enables tissue-level flexible nanoelectronics that reduce immune responses and probe drifting. As a result, it is possible to track the electrical activity of the same neurons in animals over a long period of time[12]. Despite remarkable progress, this aggressive downscaling of the neural probe dimensions due to the intrinsic stiffness of materials used in flexible nanoelectronics limits the ability to scale up the number of electrodes while maintaining tissue-level flexibility[6,17,18].

Here we introduce a spatiotemporally scalable neural probe (Fig. 1a) through the 3D integration of thin-film tissue-level soft microelectrode arrays (Fig. 1b). We have overcome the intrinsic instability of soft dielectric elastomers as passivation layers in physiological solutions through the use of fluorinated elastomers with high hydrophobicity[19] and low molecular solubility[20,21], which substantially reduces ion diffusion from surrounding biofluids, enabling a very long-term stable dielectric performance in biofluids. Specifically, we developed an elastomer based on perfluoropolyether (PFPE) as an elastic photo-patternable dielectric material[22,23]. This PFPE-based photo-patternable dielectric material is (1) 10,000 times softer than conventional stiff plastic encapsulation while maintaining the same level of longitudinal dielectric performance, (2) capable of micrometre-resolution 3D photolithographic multilayer nanofabrication and (3) compatible with nanometre-thick metal deposition. The 3D stacked microelectrode arrays can increase the number and density of electrodes through 3D stacking while maintaining tissue-level flexibility and mechanical robustness, and are capable of stably tracking electrical activities at single-unit-single-spike resolution over months with reduced immune responses, which demonstrates their scalability in both spatial and temporal scales for neural electrophysiology (Fig. 1c).

Our design is based on the following rationales. One way to increase the electrode density without changing the probe's flexibility properties is by substantially reducing the interconnect dimensions. However, this poses challenges such as crosstalk and signal attenuation (Supplementary Discussion 1)[24]. Another approach involves using thin-film transistors for on-site multiplexing to increase the electrode density, but their mechanical rigidity and need for thick inorganic passivation in physiological solutions[25] limit their potential for use in tissue-level flexible neural probes. A third option is to increase the electrode density by vertically stacking 3D electrode arrays (Fig. 1d)[6,13], although this requires the incorporation of low-modulus electronic materials to preserve the overall flexibility.

Although certain soft conductors[26–36] offer mechanical flexibility, their conductivity is affected to a large extent by their softness (Fig. 1e). The moderate conductivity compounded with large parasitic capacitance limits their use in high-density neural recording[37]. To offer sufficient conductivity for signal transmission and maintain cellular-level mechanical properties and feature sizes, nanoscale metals (for example, gold (Au)) are still the ideal candidates for interconnects (Fig. 1e,f, Extended Data Fig. 1 and Supplementary Discussion 2). By contrast, the dielectric constant (ε) that determines the performance of the encapsulation layer is not always affected by the mechanical softness of the insulator. Using an Euler–Bernoulli beam theory-based analytical model (Supplementary Discussion 3), we found that combining a soft dielectric elastomer as the encapsulation layer with a nanometre-thick metal layer as the conductive layer can substantially reduce the flexural rigidity of the neural probe (that is, the bending stiffness per unit width) by around 10,000 times (Fig. 1g and Extended Data Fig. 2a–e) compared with the probe using rigid plastic encapsulation. In fact, the contribution of the elastomer layers to the overall probe flexural rigidity is negligible compared with that of a frictionless stack of nanometre-thick metal layers alone. Therefore, incorporating thin-film dielectric elastomers with tissue-level elastic modulus as passivation layers could pave the way to increase further the electrode count and density in tissue-like electronics through 3D stacking (Fig. 1b,c).

Long-term stable soft encapsulation in biofluids

Conventional dielectric elastomers can be used as soft encapsulation materials for bioelectronics; however, their long-term encapsulation performance is limited by the progressive penetration of ions[37] from physiological solutions into the elastomer (Fig. 1h,i). Our previous work showed that their electrochemical impedance drops drastically in biofluids, reducing the cut-off frequency of the encapsulated electrode[37] (Extended Data Fig. 1). This instability is caused mainly by the diffusion of ions from biofluids into the elastomers (Fig. 2a) as soft polymers have molecular permeabilities that are typically orders of magnitude higher than those of plastics and inorganics[38–40]. The ionic

Fig. 2 | Fluorinated elastomers as soft and long-lived dielectrics. **a**, Schematics showing the effect of ion diffusion and solvent swelling on a plastic, a conventional elastomer and a fluorinated elastomer. **b**, Diffusion coefficient of water (top) and sodium and chloride ions (bottom) as a function of 1,000/T estimated via MD simulations for PDMS, H-SEBS, perfluoropolyether dimethacrylate (PFPE-DMA) and poly(1,1,1,3,3,3-hexafluoroisopropyl acrylate) (PHFIPA), where the values are shown as the mean ± s.d. for $n = 5$ simulations per material and per diffusing species. **c**, Schematics illustrating the electrochemical methods used to evaluate the built-up ionic conductivity of dielectric polymers after immersion in physiological solution (middle). Left: three-electrode setup used to measure the EIS spectrum, which determines the impedance of the dielectric polymer. The working electrode is in contact with one side of the dielectric thin film, while the other side is immersed in PBS with the Pt counter electrode and the reference Ag/AgCl electrode. The electrochemical impedance across the dielectric thin film is measured over the time course of immersion in PBS. Right: EEC measurement, in which the dielectric polymer thin films, previously soaked in PBS, are transferred to deionized (DI) water to measure the concentration of ions released from the polymer into the solution using conductimetry. **d**, Modulus of the normalized electrochemical impedance of various dielectric films at 1 Hz after soaking in 10x PBS at 70 °C at $t/H^2 = 5$ d μm^{-2} (except for PDMS, with $t/H^2 = 1.55$ d μm^{-2}). For the SU-8, PFPE-DMA, PHFIPA, PPFHEA, H-SEBS and PDMS samples, $n = 4, 4, 4, 4, 12$ and 8, respectively, where the values are shown as the mean ± s.d., using one-way ANOVA (analysis of variance) with Dunnett's multiple comparison test and SU-8 as the control group. (The values obtained for each measurement are shown by the filled grey symbols.) ***$P < 0.001$; ****$P < 0.0001$; N.S., not significant. **e**, Concentration of ions released in DI water per polymer volume as a function of t/H^2 at 4, 37 and 65 °C during EEC measurements. **f**, Comparison of the ionic conductivity of dielectric polymers soaked in 1x PBS at 37 °C obtained using both measurement methods. For EIS, we show our previously reported results for PDMS and H-SEBS (mean ± s.d.)[37] and compare them with the data obtained for PFPE-DMA and SU-8 in this work ($n = 4$ samples for each material, mean ± s.d.). **g**, Modulus of electrochemical impedance for the PFPE-DMA and SU-8 thin films in 1× PBS at 37 °C as a function of the soaking time. Average thicknesses are 1 μm for the PFPE-DMA films and 800 nm (a double layer of two 400-nm-thick films to reduce pinholes) for the SU-8 films ($n = 4$ samples for each material, and data are shown as the mean ± s.d.). **h**, Nominal stress–stretch curves for the dielectric polymer films. Only a subset of the entire stress–stretch curve is shown for SU-8, PI and H-SEBS. Inset: schematic of the mechanical testing of a polymer sample in pure shear geometry. **i**, Elastic modulus against $t_{1/2}/H^2$ (which corresponds to the time required to decrease the initial modulus of the normalized impedance by 50%) measured at 1 kHz when soaked in 1x PBS at 37 °C for the different dielectric polymers. Individual data points for PDMS and H-SEBS were obtained from our previous work[37]. Values shown are the mean ($n = 4$ samples) for PI, PFPE-DMA and SU-8. The values for PFPE-DMA and SU-8 are higher than 500 d μm^{-2}.

https://doi.org/10.1038/s41565-023-01545-6

conductivity of polymers is directly proportional to their diffusivity and solubility (equation (1)),

$$\sigma = 2\frac{q^2}{kT}D \times S \times C_{\text{out}} \quad (1)$$

where σ is the ionic conductivity, q is the elementary charge, k is the Boltzmann constant, T is the temperature, D is the ionic diffusivity, S is the ionic solubility and C_{out} is the concentration of ions in the surrounding biofluids at equilibrium (Supplementary Discussion 4). Notably, because ionic diffusivity in standard dielectric elastomers is in the range of 10^{-15} to 10^{-17} m^2 s^{-1} at 37 °C, this instability can only be observed in micrometre-thick dielectric films over a timescale of days to weeks, which is critical for long-term neural recording.

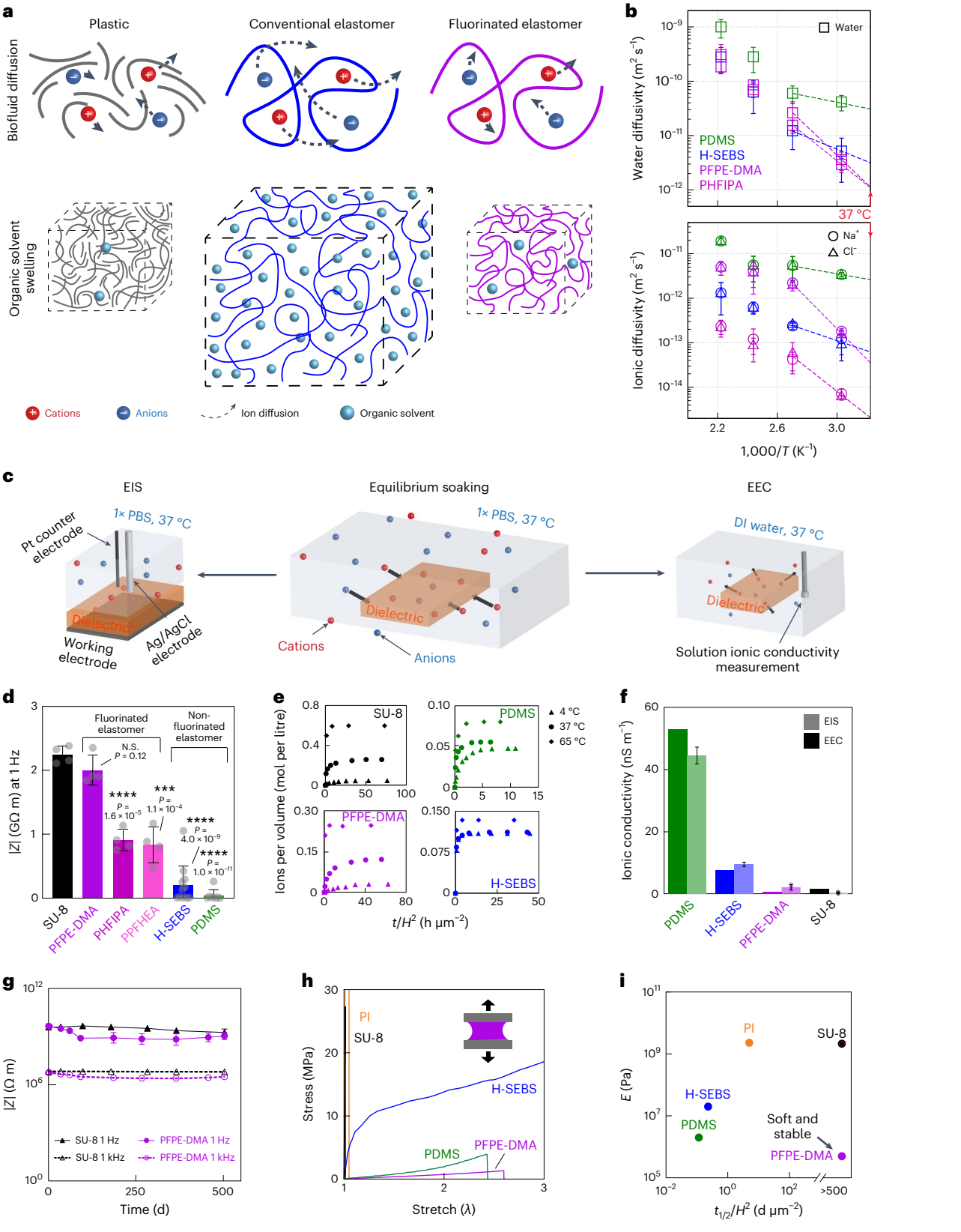

We used molecular dynamics (MD) simulations to study the diffusion of water and sodium chloride across different dielectric elastomers to better understand this ion-diffusion process and identify material systems that could potentially solve this issue (see Methods, Extended Data Fig. 3 and Supplementary Tables 1 and 2). Our MD simulations revealed that, towards 37 °C, the molecular diffusivity of water and sodium and chloride ions in fluorinated elastomers (PFPE-DMA and PHFIPA) is lower than that in conventional elastomers (PDMS and H-SEBS) (Fig. 2b). This lower diffusivity suggests that fluorinated elastomers can have a lower ionic conductivity (Supplementary Discussion 4 and equation (1)) than conventional elastomers, which could allow them to maintain their dielectric performance during long-term immersion in physiological solutions. To test this hypothesis, we systematically characterized the long-term electrochemical stability of eight different dielectric materials, which comprised three fluorinated elastomers (PFPE-DMA, PHFIPA and poly[2-(perfluorohexyl)ethyl] acrylate (PPFHEA)), three non-fluorinated elastomers (PDMS, H-SEBS and polyisobutylene (PIB)) and two plastic dielectric polymers (polyimide (PI) and SU-8 2000.5 (SU-8)) as controls.

We evaluated the ionic conductivity of the dielectric polymers (see Methods, Supplementary Discussion 5 and Supplementary Table 3) (Fig. 2c) using electrochemical impedance spectroscopy (EIS)[37] (Extended Data Fig. 4a–c) and external electrolyte conductimetry (EEC) techniques (Extended Data Fig. 5a,b). We used an electrical model of the dielectric material with conductive losses to estimate the ionic conductivity from EIS data (Extended Data Fig. 4a–c and Supplementary Table 4)[37,41]. To conduct an accelerated ageing test, we soaked the polymer thin films in 10x PBS solution at 70 °C. Bode plots of normalized electrochemical impedance (Z) before and after soaking (Extended Data Fig. 4d) showed substantial impedance reduction for the conventional elastomer and PI films across the 0–1,000 Hz range, whereas SU-8 and the fluorinated elastomer films exhibited a slight decrease. At low frequency (<1,000 Hz), all of the fluorinated elastomer films showed a lower impedance modulus drop than the PDMS, H-SEBS, PIB and PI films. To account for variations in diffusion times due to differences in thickness among the samples (Supplementary Table 4), we plotted the progressive decrease in impedance modulus at 1 Hz and 1 kHz (Fig. 2d and Extended Data Fig. 4e,f) as a function of the time (t) normalized by the square of the average thickness (H) of the polymer films. A larger reduction in normalized impedance is observed for the non-fluorinated elastomers at 1 Hz. In addition, we extrapolated average dielectric constants of the dielectric thin films in the frequency range of 1,000–100,000 Hz from the EIS plots (Supplementary Table 5), confirming the low dielectric constant of PFPE-DMA ($\varepsilon = 1.99 \pm 0.03$), consistent with previous reports[42,43].

Using EEC (Fig. 2c and Extended Data Fig. 5a), we further analysed the ionic diffusivity, solubility and conductivity of four representative dielectric polymers, excluding the remaining polymers due to sample-preparation limitations (see Supplementary Discussion 5 and Supplementary Table 3). The ionic conductivity changes in DI water indicate the ion-diffusion rates from these polymers (Fig. 2e). The value of the plateau in the solution's conductance is proportional to the ionic solubility, S. We determined the ionic diffusivity, D, by fitting the experimental data (see Supplementary Discussion 5 and Extended Data Fig. 5b,c) and calculated ionic conductivity using equation (1). The results from both methods[37] (Fig. 2f and Supplementary Table 6) consistently showed that the ionic conductivity of PFPE-DMA is similar to that of SU-8 but 1–2 orders of magnitude lower than the other dielectric elastomers. This reduced ionic conductivity is mostly attributed to its low ionic diffusivity (Extended Data Fig. 5d and Supplementary Table 6), aligning with MD simulations.

We carried out EEC measurements at different temperatures to calculate the average ion-diffusion activation energy and the heat of solution between 4 and 65 °C (refs. 44–46) (Extended Data Fig. 5e–g and Supplementary Table 7). The average activation energy for PFPE-DMA is even higher than SU-8, and its enthalpy of the solution is closer to SU-8 but higher than hydrocarbon elastomers. This aligns with our MD simulations showing low ionic diffusivity in PFPE-DMA (Fig. 2b). The MD simulations suggested a correlation between ionic diffusivity and polymer density (Extended Data Fig. 3c,d), but further simulations to analyse the molecular mechanism of diffusion are required to understand the difference between fluorinated and hydrocarbon elastomers. In addition, PFPE-DMA has a low water permeability (Supplementary Table 8), comparable to that of PIB, which could contribute to its long-term stability in biofluids.

Our results highlighted the stability of the dielectric performance of fluorinated dielectric elastomers in biofluids. We further tested PFPE-DMA as a long-lived dielectric material for implantable bioelectronics, given its potential in nanofabrication[22,23]. The results showed that the PFPE-DMA film is as stable as the SU-8 double layers over a soaking period of 17 months (Fig. 2g). Notably, the elastic modulus of the crosslinked PFPE-DMA film is 0.50 MPa, which is approximately 10,000 times softer than SU-8 (Fig. 2h and Extended Data Fig. 6a–e). We plotted the elastic modulus against the half-life time ($t_{1/2}$) of the thin-film dielectric impedance at 1 kHz, which is defined as the soaking time required for the initial impedance modulus to decrease by 50% (Extended Data Fig. 4f). PFPE-DMA uniquely combines both mechanical softness and long-term dielectric performance stability (Fig. 2i), making it ideal for implantable neural probes in spatiotemporally scalable in vivo electrophysiology.

3D scalable neural probes

We developed a 3D photolithographic protocol using PFPE-DMA elastomers for scalable neural probe fabrication. Traditional elastomers are not suitable for multilayer photolithography as the organic solvents used in the process[21,47] easily cause the elastomers to swell, damaging the thin-film microstructures and microelectronic components. PFPE-DMA elastomers, however, have demonstrated chemical orthogonality[20,48], resisting both organic and aqueous solvents, preserving their surface even after intensive nanofabrication. However, the high contact angle with other conventional photo-patternable dielectric materials and the low surface adhesion energy to metals prevent the direct patterning of metals on PFPE-DMA elastomers. In addition, sensitivity to oxygen during crosslinking limits the resolution of mask-based photolithographic patterning of PFPE-DMA elastomers. To overcome these challenges, we developed the following technological advancements: (1) a 3D-printable nitrogen diffuser integrated with conventional photoaligners to create an inert atmosphere during exposure to ultraviolet (UV) light, enabling microscale photopatterning of PFPE-DMA (Extended Data Fig. 7a–c); (2) a photopatterned

Fig. 3 | 3D integration of high-density soft microelectrode arrays for scalable neural probes. a, Schematics showing the stepwise nanofabrication process of a multilayer neural probe encapsulated by PFPE-DMA elastomers. **b**, Photograph of PFPE-DMA elastomer-encapsulated neural probes with four layers of electrode arrays self-wrapping on a glass capillary. **c**, BF micrograph of the neural probe in **b**. **d**, Expanded merged BF micrograph of the region in **c** highlighted by the black box. **e**, Focused ion beam (FIB) combined with SEM image showing the cross-section of the region in **c** highlighted by the blue box. Each layer is pseudo-coloured and labelled. **f**, Change in the impedance modulus at 1 kHz before and after electroplating with Pt black or PEDOT:PSS for 40-μm-diameter electrodes of neural probes ($n = 32$). The data in the bar plots show the mean ± s.d. and the grey dots show the values obtained for individual electrodes. ****$P < 0.0001$, two-tailed, paired t-test. **g**, Electrodes per cross-sectional area of state-of-the-art neural probes as a function of the elastic modulus of the dielectric encapsulation[6,11–13,17,35,54,55]. Inset: schematic of a neural probe's cross-section with width W, height H and $N = 8$ electrodes.

https://doi.org/10.1038/s41565-023-01545-6

spacer to prevent direct contact between the PFPE-DMA precursor and the photomask, preserving the nanometre smoothness of the PFPE-DMA film during photolithography (Extended Data Fig. 7d,e); (3) treatment with an inert gas plasma to decrease the contact angle of the photoresists and increase adhesion to other materials (Extended Data Fig. 7f–h); and (4) high-pressure sputtering of metal oxide/metal layers to deposit metal lines and prevent metal-ion diffusion into PFPE-DMA. Processes (1)–(4) can be repeated to create multilayered microelectronic structures. Importantly, these innovations enable PFPE-DMA to be processed as a negative photo-patternable dielectric material

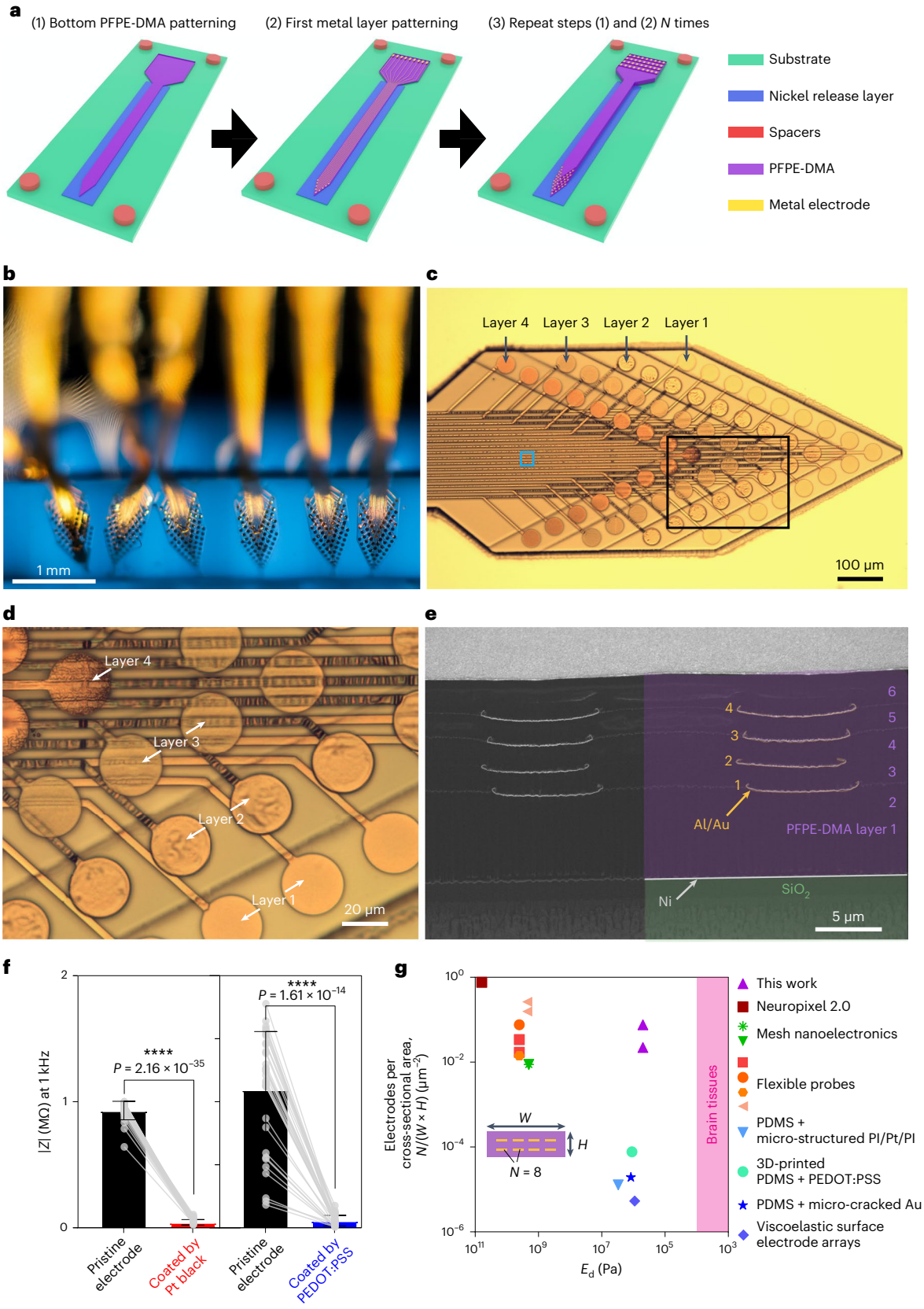

in a standard cleanroom, establishing PFPE-DMA as an elastomer that is compatible with conventional photolithographic processes for 3D electronics (Fig. 3a, Extended Data Fig. 7a and Methods).

Figure 3b shows the flexibility of a neural probe with 64 electrodes on a glass capillary (Extended Data Fig. 8a–c). The corresponding bright-field (BF) optical image shows one probe containing six layers of PFPE-DMA sandwiching four layers of metal electrodes (Fig. 3c,d and Extended Data Fig. 8d–i). Scanning electron microscopy (SEM) imaging (Extended Data Fig. 8h–k) is used to confirm the smooth surface of the PFPE-DMA dielectric layers after the ten-layer fabrication process. We achieved a lateral resolution of approximately 1 µm for the PFPE-DMA features (Extended Data Fig. 8d–l), and surface treatment enabled standard photoresists to define precise features on the PFPE-DMA film (Extended Data Fig. 8g–i,l). Notably, there was no delamination between the PFPE-DMA and metal layers (Fig. 3e and Extended Data Figs. 8m–o and 6n–t), even after a uniaxial stretch to 20% (Extended Data Fig. 8o). Adhesion testing[49,50] (Extended Data Fig. 6f–k) showed that the self-adhesion energy of the PFPE-DMA layers was substantially higher than their adhesion energy to a glass substrate and was closer to their intrinsic fracture toughness measured (Extended Data Fig. 6e), indicating that the two PFPE-DMA layers adhere strongly and do not delaminate easily under strain. Delamination between layers was not observed on the 64-channel, four-metal-layer neural probes after >20% of uniaxial stretch (Extended Data Fig. 6l). In addition, accelerated ageing in saline did not induce delamination between the PFPE-DMA and metal layers (Extended Data Fig. 6n–t).

We measured the conductivity of the metal interconnects and electrodes on PFPE-DMA as a function of their aspect ratio (Extended Data Fig. 8p), and found average conductivity values consistent with standards for sputtered Al/Au (40/100 nm) metal lines. Our fabrication method is compatible with three-inch wafer-scale fabrication processes (Extended Data Fig. 8q). To facilitate connections to recording setups, we overexposed the PFPE-DMA layers to create smooth steps at their edges and used isotropic metal deposition to continuously deposit the metal electrodes from different PFPE-DMA layers to the input/output (I/O) pads, enabling standard flip-chip bonding of flexible cables (Extended Data Fig. 7i–m). Finite element analysis indicated that the strain concentration in the central metal layer remains below the yield strain of Au when bent (Extended Data Fig. 2f–h), suggesting that metal interconnects will not undergo plastic deformation or fracture. The adhesion of the metal lines to the elastomer is even sufficient to generate wrinkle patterns, which are commonly observed in laminates[34,51] (Fig. 3d and Extended Data Fig. 8g–i) with a stiff island on a soft substrate, where larger strains can be accommodated before failure of the stiff layer compared with the free-standing fracture strain[51–53]. This result can explain further why metal lines are still highly conductive after 5% uniaxial strain (Extended Data Fig. 6m).

After chip bonding, we used standard electroplating techniques to coat the electrode tips with poly(3,4-ethylenedioxythiophene) polystyrene sulfonate (PEDOT:PSS) or platinum black (Pt black) to verify the conductivity of the electrodes (see Methods and Extended Data Fig. 8r,s). The reduced electrochemical impedance matches previously reported values and is comparable to other implantable brain probes[6,12,13] (Fig. 3f). We also conducted chronic measurements of the impedance of sputtered Al/Au interconnects and Pt electrodes to confirm the stability of fluorinated elastomer-based neural probes without additional effects from the electroplated material (Extended Data Fig. 8t). Finally, we showed that the crosstalk level between neighbouring electrodes in a relevant test geometry was comparable to standard values measured in polymer microelectrode arrays after more than 50 days of soaking time in 1x PBS (Extended Data Fig. 4g–j)[24]. Collectively, compared with state-of-the-art neural probes made with other soft materials and thin-film plastic passivation, PFPE-based neural probes, respectively, increase the density of the electrodes by over two orders of magnitude (up to 7.6 electrodes per 100 µm^2 of the cross-section in this work)[35,54–56] and increase the mechanical softness by between three and five orders of magnitude (Fig. 3g and Supplementary Table 9)[6,11–13,17,57,58].

Multilayer neural probes encapsulated by dielectric elastomers are still more flexible than probes made with plastic dielectric materials. Comparing neural probes made using 9-µm-thick PFPE-DMA or SU-8, the PFPE-DMA-based probes exhibit substantially higher flexibility (Extended Data Fig. 2f–h). Finite element analysis confirms the difference in their flexibility to be due to the different elastic modulus values between the elastomeric and rigid dielectric materials. Specifically, the SU-8 layer is the principal load-carrying member in the SU-8-based probe, whereas in the PFPE-DMA-based probe, the PFPE-DMA layer contributes negligibly to the load-carrying capacity. Instead, the nanometre-thick metal layer is the principal load-carrying member. As a result, a simple beam model with three electrode layers shows that this design reduces the contribution of the encapsulation layers to the overall flexural rigidity of the neural probe by a factor of 900 (Extended Data Fig. 2b).

Long-term stable neural electrophysiology

We implanted neural probes in the mouse brain for chronic recording. The soft neural probes were delivered into the brain following the previously reported method (Extended Data Fig. 9a–c and Methods)[59]. The PFPE-DMA probes have four-layer electrode arrays vertically integrated, with a cross-sectional area approximately 150–500 times larger than that of an ultraflexible probe[17,18], thus enabling a high density of 64 electrodes to be packed in one probe (Fig. 4a), and they were implanted in the somatosensory cortex and connected to a voltage amplifier through a flat flexible cable for electrophysiological recording (Extended Data Fig. 9d and Methods).

We compared the brain immune response of multilayer PFPE-DMA probes with SU-8 probes of the same thickness (Fig. 4b,c). At twelve weeks post-implantation, we observed a significant enhancement of the NeuN (neuron) signal around the PFPE-DMA probes compared with the SU-8 probes. In addition, the fluorescence intensity of astrocytes

Fig. 4 | Long-term stable brain electrophysiology and implantation with reduced immune responses by scalable soft neural probes. a, BF image of a multilayer, high-density PFPE-DMA neural probe with four layers of electrode arrays and 64 channels after Pt black electrodeposition. **b**, Representative immunostaining of horizontal brain slices at two (top), six (middle) and twelve weeks (bottom) post-implantation. The green, pink, cyan, blue and red colours show signals corresponding to neurons (NeuN), astrocytes (GFAP), microglia (IBA1), the DAPI dye and rhodamine 6G-stained devices, respectively. The PFPE-DMA ('Soft brain probe') and SU-8 ('Flexible brain probe') probes are both 9 µm thick and 250 µm wide. **c**, Normalized average fluorescence intensity of NeuN, GFAP and IBA1 signals as a function of distance from the probe–tissue interfaces at two, six and twelve weeks post-implantation. The fluorescence intensity at 500–525 µm away from the probe was used for normalization ($n = 4$ brain slices, mean ± s.e.m., $^*P < 0.05$; $^{**}P < 0.01$, $^{***}P < 0.001$, two-tailed unpaired t-test for distance between 0 and 250 µm away from the probe). **d**, Left: representative voltage traces (300–3,000 Hz bandpass filtered) recorded from a high-density PFPE-DMA neural probe at four weeks post-implantation. Right: unit activities of the region highlighted by the dashed red box in the left panel. **e**, Average single-unit waveforms detected in **d**. **f**, Representative ISI plots over ten weeks of recording. Each plot corresponds to a unit tracked on the same electrode. **g**, Representative average waveforms from two to ten weeks post-implantation. **h**, Clusters of the waveforms detected in **g** in PCA space as a function of the number of weeks post-implantation. PC1 and PC2 represent the first two axes in the PCA from the clustering algorithm. In **g** and **h** the same colour is used for corresponding average waveforms (**g**) and clusters (**h**). **i**–**k**, Peak–valley amplitude (**i**), firing rate (**j**) and waveform similarity (**k**) of the units detected in **g** and **h** as a function of the post-implantation time ($n = 14$ units, mean ± s.d.).

https://doi.org/10.1038/s41565-023-01545-6

and microglia at twelve weeks post-implantation was significantly reduced around the PFPE-DMA probes in comparison with the SU-8 probes. However, the difference in the microglia signals was marginal. These results demonstrate that the 3D vertically stacked, multilayer PFPE-DMA probes can maintain long-term biocompatibility with the brain tissue.

Chronic recording (Fig. 4d,e) showed that single-unit action potentials were recorded stably over an implantation period of ten weeks, with minimal change in the interspike interval (ISI) distribution (Fig. 4f) and waveform shape (Fig. 4g). Moreover, principal component analysis (PCA) showed that all units exhibited nearly constant positions on the first and second principal component plane (PC1–PC2) from two

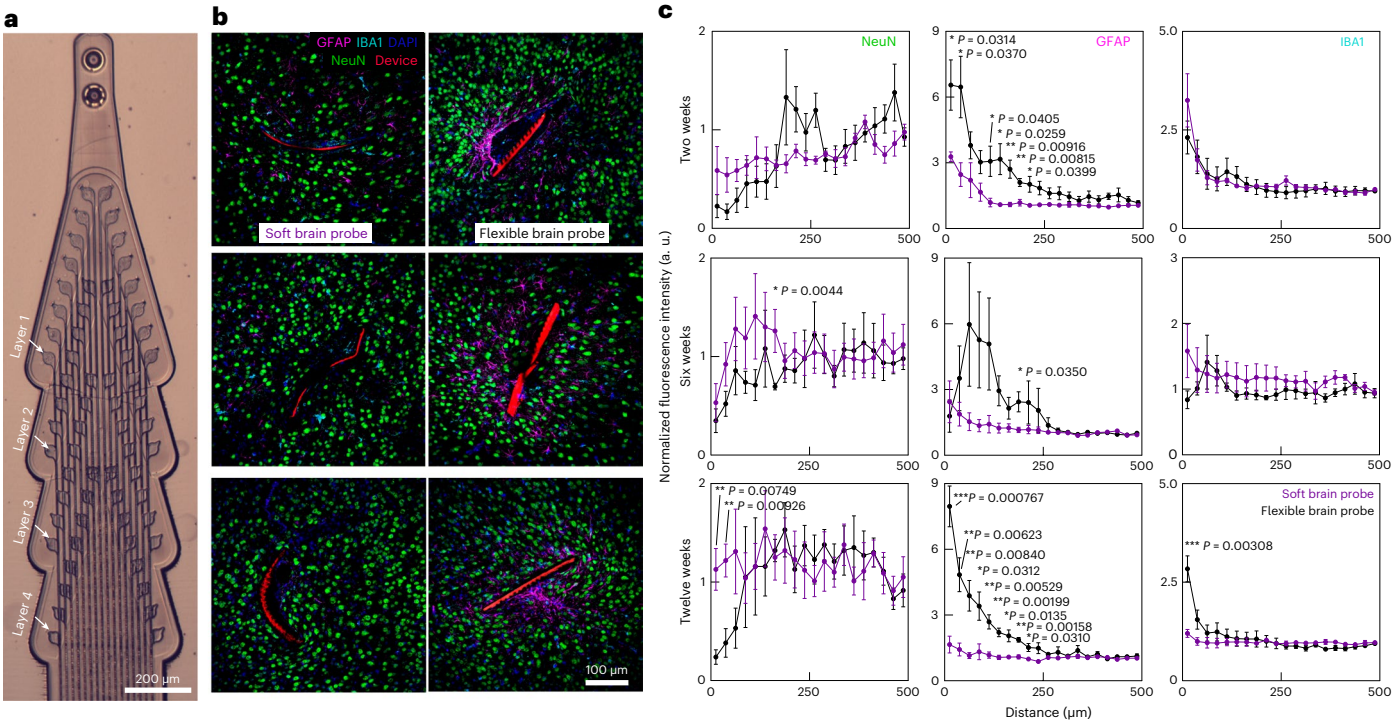

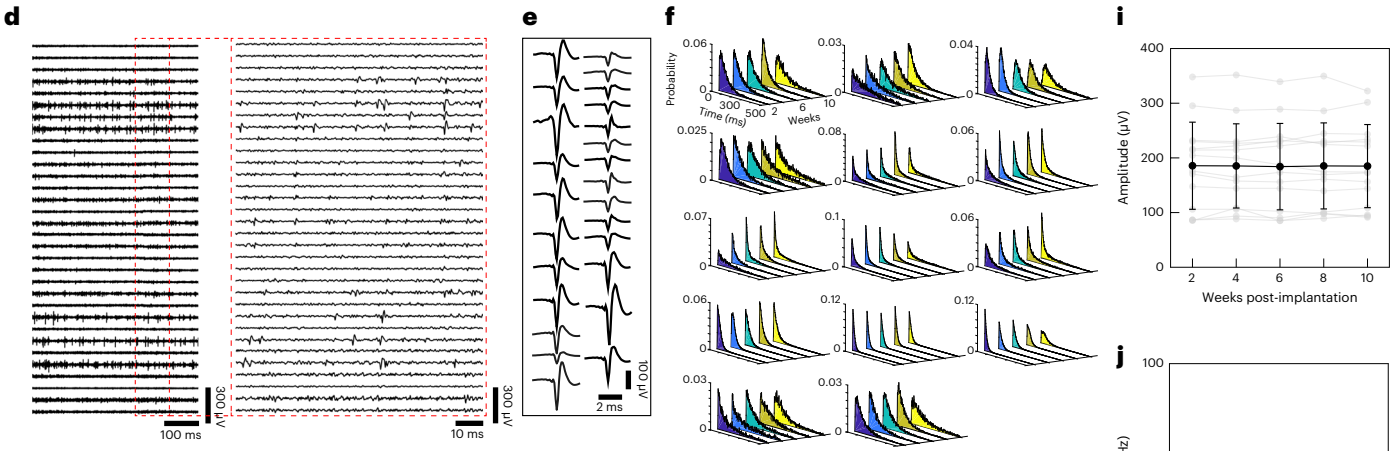

https://doi.org/10.1038/s41565-023-01545-6

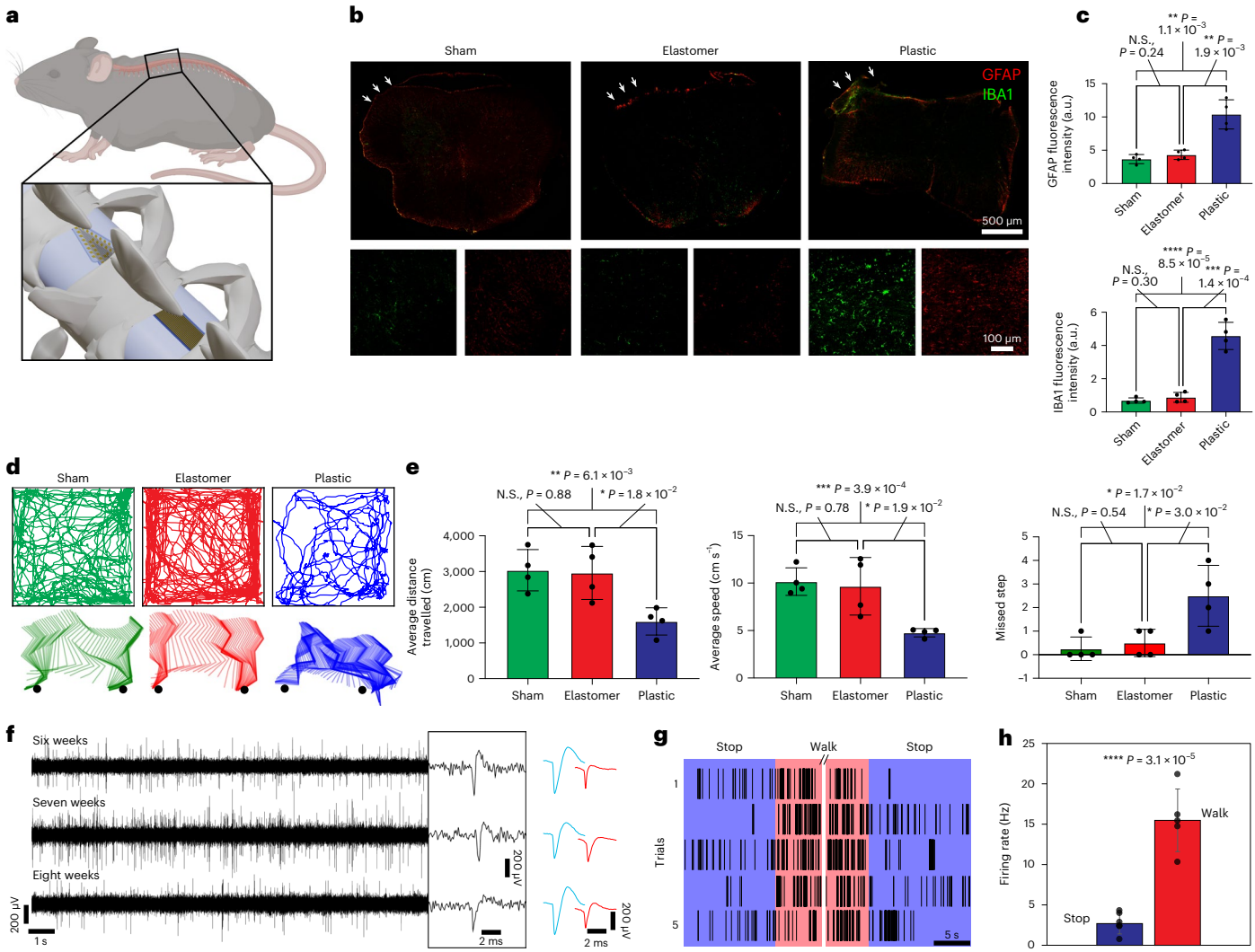

Fig. 5 | Long-term stable spinal cord recording. a, Schematic of the spinal cord-implanted mice. **b**, Representative confocal fluorescence images showing GFAP (astrocytes) and IBA1 (microglia) staining in the sections of spinal cord tissues from sham control mice (left) and mice implanted with PFPE-DMA (elastomer, middle) and PI (plastic, right) probes at six weeks post-implantation. The insets show expanded panels to highlight the contact area with the implanted neural probes. **c**, Bar plots showing the statistical summary of the astrocyte (top) and microglia (bottom) fluorescence intensities in the regions of interest, where the spinal cord tissues received sham surgery or were implanted with neural probes (white arrows in **b**). $^{*}P < 0.05$; $^{**}P < 0.01$, $^{***}P < 0.001$, $^{****}P < 0.0001$, N.S. not significant, two-tailed unpaired *t*-test. Data were obtained for $n = 4$ independent biological replicates, mean ± s.d. **d**, Top: representative data showing the motion traces for a sham control animal (green) and animals implanted with PFPE-DMA (red) and PI (blue) neural probes at four weeks post-implantation. Bottom: representative data showing the hindlimb kinematics. Black circles represent the bars of the ladder on which the animals walked. **e**, Bar plots summarizing the average distance travelled (left), average movement speed (middle) and number of missed steps onto the rungs of the ladder (right) for the motion-trace characterization ($n = 4$ independent experiments, mean ± s.d., two-sided, unpaired *t*-test) at four weeks post-implantation. **f**, Left: voltage traces (filtered in the 250–3,000 Hz range) of a representative channel showing spike-like electrical activity from post-implantation periods of six to eight weeks. Middle: expansion showing the representative spike-like electrical signals. Right: Sorted spiking units identified from the left panel. Red and blue colours are used to distinguish two average waveforms detected on a representative electrode. **g**, Raster plot of spike-like signals in a representative channel during mouse resting and walking states. **h**, Average firing rate between animal walking and resting states ($n = 5$ and 6 trials for walking and resting states, respectively, $^{****}P < 0.0001$, two-tailed unpaired *t*-test). Panel **a** created with BioRender.com.

to ten weeks post-implantation (Fig. 4h). In addition, the amplitude, firing rate and waveform similarity remained constant over all the recording sessions, suggesting that the high-density, multilayer soft probe could stably track the activity from the same neurons over time (Fig. 4i–k). We also confirmed the stability of brain recording using a PFPE-DMA probe with a single-layer electrode array (approximately 2-μm-thick PFPE-DMA) to further validate the dielectric stability of the ultrathin PFPE-DMA encapsulation layer during chronic brain recording (Extended Data Fig. 10).

The stretchability of the PFPE-DMA dielectric layer enables the multilayer neural probe to tolerate more strain and introduce less mechanical damage to the tissue during the bending. To demonstrate this, we performed chronic electrophysiology on the mouse spinal cord (Fig. 5a and Methods). We first characterized the long-term immune response by comparing the immune response from PFPE-DMA and PI probes with that of sham-operated controls (Methods). PI probes of 25 μm thickness were used as standard for flexible spinal cord implants[60], which are robust enough to withstand the surgical procedure and chronic implantation. The sham-operated group of animals received spinal cord surgery but no device implant. Neuroinflammatory responses at chronic stages were evaluated by the density of astrocytes (GFAP) and microglia

(IBA1) for foreign-body reactions, which showed that the density of astrocytes and microglia increased in the vicinity of PI probes at six weeks post-implantation. By contrast, there was no significant difference between mice with PFPE-DMA probes and sham-operated animals (Fig. 5b,c).

We characterized the impact of implantation on animal behaviours by measuring freely moving mice in an open-field box and whole-body movement during basic walking and skilled locomotion across a horizontal ladder (Fig. 5d). Statistical results showed that, compared with sham controls, mice implanted with PI probes showed a reduction in the average distance travelled and average speed during movements, as well as motor deficits, whereas mice implanted with the PFPE-DMA probes showed no significant differences (Fig. 5e). Using the implanted electrodes, we recorded the spike-like electrical activity from the representative electrodes over several weeks (Fig. 5f), with changes in firing rate corresponding to the animal resting and walking states (Fig. 5g,h). The observed spikes exhibit prolonged durations (2–4 ms) and heightened amplitudes (250–500 μV). This phenomenon has been noted previously in depth probe spinal cord recordings of mice[60]. However, further investigation is required to determine if these spikes are indicative of multi-unit action potentials or local field potentials. These results show that PFPE-DMA soft neural probes implanted in the mouse spinal cord do not affect the animal behaviour and can provide a stable recording of spinal cord electrical activity.

Conclusion

Our results showed that neural probes can be made with four layers of fluorinated elastomer/metal structures. An analytical model based on Euler–Bernoulli beam theory (Supplementary Discussion 3) shows that probes with up to nine layers have a flexural rigidity below 1 μN m, whereas probes encapsulated by plastic dielectrics with only three layers of electrodes have a flexural rigidity above 1 μN m (Extended Data Fig. 2b,c). In practice, plastic probes thicker than 10 μm are brittle, whereas elastomer-encapsulated probes remain flexible and robust for implantation (Supplementary Video 1).

It has been demonstrated that ultrasoft neural probes with larger cross-sections can achieve long-term stable neural recordings compared with thin rigid plastic probes[17,18]. These ultrasoft probes can support more channels. We recognize that the extreme modulus mismatch between the Au and PFPE-DMA layers may lead to a split of the neutral axis[61], which could reduce the flexural rigidity. However, an analytical model based on previous work[62] indicates that Euler–Bernoulli theory still applies to the majority of the probe's length (see Supplementary Discussion 3 and Extended Data Fig. 2d,e). In practice, the main limitations in scaling these probes will probably come from microfabrication challenges (see Supplementary Discussion 6).

When the elastic modulus of the dielectric layer is below the megapascal level, its contribution on the total flexural rigidity of the probe is minimal and metal layers dominate the probe's mechanical properties. Therefore, as the number of layers increases, the benefit decreases asymptotically because the metal layers located further from the neutral axis contribute more to the flexural rigidity of the probe (Extended Data Fig. 2a and Supplementary Discussion 3). To reduce this rigidity, strategies, such as adjusting the metal-layer placements, increasing the outer elastomer thickness to prevent signal leakage or using softer conductors such as liquid metal[63], can be considered.

Online content

Any methods, additional references, Nature Portfolio reporting summaries, source data, extended data, supplementary information, acknowledgements, peer review information; details of author contributions and competing interests; and statements of data and code availability are available at https://doi.org/10.1038/s41565-023-01545-6.

References

1. Sadtler, P. T. et al. Neural constraints on learning. *Nature* **512**, 423–426 (2014).
2. Gallego, J. A., Perich, M. G., Chowdhury, R. H., Solla, S. A. & Miller, L. E. Long-term stability of cortical population dynamics underlying consistent behavior. *Nat. Neurosci.* **23**, 260–270 (2020).
3. Perlmutter, J. S. & Mink, J. W. Deep brain stimulation. *Annu. Rev. Neurosci.* **29**, 229–257 (2006).
4. Patel, S. R. & Lieber, C. M. Precision electronic medicine in the brain. *Nat. Biotechnol.* **37**, 1007–1012 (2019).
5. Adolphs, R. The unsolved problems of neuroscience. *Trends Cogn. Sci.* **19**, 173–175 (2015).
6. Musk, E. An integrated brain–machine interface platform with thousands of channels. *J. Med. Internet Res.* **21**, e16194 (2019).
7. Lacour, S. P., Courtine, G. & Guck, J. Materials and technologies for soft implantable neuroprostheses. *Nat. Rev. Mater.* **1**, 16063 (2016).
8. Jun, J. J. et al. Fully integrated silicon probes for high-density recording of neural activity. *Nature* **551**, 232–236 (2017).
9. Tooker, A. et al. Optimization of multi-layer metal neural probe design. *Conf. Proc. IEEE Eng. Med. Biol. Soc.* **2012**, 5995–5998 (2012).
10. Salatino, J. W., Ludwig, K. A., Kozai, T. D. Y. & Purcell, E. K. Glial responses to implanted electrodes in the brain. *Nat. Biomed. Eng.* **1**, 862–877 (2017).
11. Liu, J. et al. Syringe-injectable electronics. *Nat. Nanotechnol.* **10**, 629–636 (2015).
12. Yang, X. et al. Bioinspired neuron-like electronics. *Nat. Mater.* **18**, 510–517 (2019).
13. Chung, J. E. et al. High-density, long-lasting, and multi-region electrophysiological recordings using polymer electrode arrays. *Neuron* **101**, 21–31 (2019).
14. Someya, T., Bao, Z. & Malliaras, G. G. The rise of plastic bioelectronics. *Nature* **540**, 379–385 (2016).
15. Khodagholy, D. et al. NeuroGrid: recording action potentials from the surface of the brain. *Nat. Neurosci.* **18**, 310–315 (2015).
16. Xie, C. et al. Three-dimensional macroporous nanoelectronic networks as minimally invasive brain probes. *Nat. Mater.* **14**, 1286–1292 (2015).
17. Luan, L. et al. Ultraflexible nanoelectronic probes form reliable, glial scar-free neural integration. *Sci. Adv.* **3**, e1601966 (2017).
18. Fu, T. M. et al. Stable long-term chronic brain mapping at the single-neuron level. *Nat. Methods* **13**, 875–882 (2016).
19. Dalvi, V. H. & Rossky, P. J. Molecular origins of fluorocarbon hydrophobicity. *Proc. Natl Acad. Sci. USA* **107**, 13603–13607 (2010).
20. Rolland, J. P., Van Dam, R. M., Schorzman, D. A., Quake, S. R. & DeSimone, J. M. Solvent-resistant photocurable 'liquid Teflon' for microfluidic device fabrication. *J. Am. Chem. Soc.* **126**, 2322–2323 (2004).
21. Liao, S., He, Y., Chu, Y., Liao, H. & Wang, Y. Solvent-resistant and fully recyclable perfluoropolyether-based elastomer for microfluidic chip fabrication. *J. Mater. Chem. A* **7**, 16249–16256 (2019).
22. Liu, J. et al. Fully stretchable active-matrix organic light-emitting electrochemical cell array. *Nat. Commun.* **11**, 3362 (2020).
23. Liu, Y. et al. Soft and elastic hydrogel-based microelectronics for localized low-voltage neuromodulation. *Nat. Biomed. Eng.* **3**, 58–68 (2019).
24. Qiang, Y. et al. Crosstalk in polymer microelectrode arrays. *Nano Res.* **14**, 3240–3247 (2021).
25. Fang, H. et al. Ultrathin, transferred layers of thermally grown silicon dioxide as biofluid barriers for biointegrated flexible electronic systems. *Proc. Natl Acad. Sci. USA* **113**, 11682–11687 (2016).
26. Grancarić, A. M. et al. Conductive polymers for smart textile applications. *J. Ind. Text.* **48**, 612–642 (2018).

27. Shoa, T., Mirfakhrai, T. & Madden, J. D. Electro-stiffening in polypyrrole films: dependence of Young's modulus on oxidation state, load and frequency. *Synth. Met.* **160**, 1280–1286 (2010).
28. Kim, Y. H. et al. Highly conductive PEDOT:PSS electrode with optimized solvent and thermal post-treatment for ITO-free organic solar cells. *Adv. Funct. Mater.* **21**, 1076–1081 (2011).
29. Yang, C. & Suo, Z. Hydrogel ionotronics. *Nat. Rev. Mater.* **3**, 125–142 (2018).
30. Minisy, I. M., Bober, P., Šeděnková, I. & Stejskal, J. Methyl red dye in the tuning of polypyrrole conductivity. *Polymer* **207**, 122854 (2020).
31. Matsuhisa, N. et al. Printable elastic conductors by in situ formation of silver nanoparticles from silver flakes. *Nat. Mater.* **16**, 834–840 (2017).
32. Sekitani, T. et al. A rubberlike stretchable active matrix using elastic conductors. *Science* **321**, 1468–1472 (2008).
33. Qu, J., Ouyang, L., Kuo, C.-C. & Martin, D. C. Stiffness, strength and adhesion characterization of electrochemically deposited conjugated polymer films. *Acta Biomater.* **31**, 114–121 (2016).
34. Matsuhisa, N., Chen, X., Bao, Z. & Someya, T. Materials and structural designs of stretchable conductors. *Chem. Soc. Rev.* **48**, 2946–2966 (2019).
35. Tringides, C. M. et al. Viscoelastic surface electrode arrays to interface with viscoelastic tissues. *Nat. Nanotechnol.* **16**, 1019–1029 (2021).
36. Yuk, H., Lu, B. & Zhao, X. Hydrogel bioelectronics. *Chem. Soc. Rev.* **48**, 1642–1667 (2019).
37. Le Floch, P. et al. Fundamental limits to the electrochemical impedance stability of dielectric elastomers in bioelectronics. *Nano Lett.* **20**, 224–233 (2020).
38. Song, E., Li, J., Won, S. M., Bai, W. & Rogers, J. A. Materials for flexible bioelectronic systems as chronic neural interfaces. *Nat. Mater.* **19**, 590–603 (2020).
39. Le Floch, P., Meixuanzi, S., Tang, J., Liu, J. & Suo, Z. Stretchable seal. *ACS Appl. Mater. Interfaces* **10**, 27333–27343 (2018).
40. Le Floch, P. et al. Wearable and washable conductors for active textiles. *ACS Appl. Mater. Interfaces* **9**, 25542–25552 (2017).
41. Bard, A. J. & Faulkner, L. R. *Electrochemical Methods: Fundamentals and Applications* (Wiley, 2000).
42. Olson, K. R. et al. Liquid perfluoropolyether electrolytes with enhanced ionic conductivity for lithium battery applications. *Polymer* **100**, 126–133 (2016).
43. Timachova, K. et al. Mechanism of ion transport in perfluoropolyether electrolytes with a lithium salt. *Soft Matter* **13**, 5389–5396 (2017).
44. Barrer, R. Permeability of organic polymers. *J. Chem. Soc. Faraday Trans.* **35**, 644–648 (1940).
45. Van Amerongen, G. Influence of structure of elastomers on their permeability to gases. *J. Polym. Sci.* **5**, 307–332 (1950).
46. Geise, G. M., Paul, D. R. & Freeman, B. D. Fundamental water and salt transport properties of polymeric materials. *Prog. Polym. Sci.* **39**, 1–42 (2014).
47. George, S. C., Knörgen, M. & Thomas, S. Effect of nature and extent of crosslinking on swelling and mechanical behavior of styrene–butadiene rubber membranes. *J. Membr. Sci.* **163**, 1–17 (1999).
48. Vitale, A. et al. Direct photolithography of perfluoropolyethers for solvent-resistant microfluidics. *Langmuir* **29**, 15711–15718 (2013).
49. Gent, A. N. Fracture mechanics of adhesive bonds. *Rubber Chem. Technol.* **47**, 202–212 (1974).
50. Wang, Y., Yin, T. & Suo, Z. Polyacrylamide hydrogels. III. Lap shear and peel. *J. Mech. Phys. Solids* **150**, 104348 (2021).
51. Lacour, S. P., Jones, J., Wagner, S., Teng, L. & Zhigang, S. Stretchable interconnects for elastic electronic surfaces. *Proc. IEEE* **93**, 1459–1467 (2005).
52. Li, T., Huang, Z., Suo, Z., Lacour, S. P. & Wagner, S. Stretchability of thin metal films on elastomer substrates. *Appl. Phys. Lett.* **85**, 3435–3437 (2004).
53. Li, T., Suo, Z., Lacour, S. P. & Wagner, S. Compliant thin film patterns of stiff materials as platforms for stretchable electronics. *J. Mater. Res.* **20**, 3274–3277 (2005).
54. Yuk, H. et al. 3D printing of conducting polymers. *Nat. Commun.* **11**, 1604 (2020).
55. Minev, I. R. et al. Electronic dura mater for long-term multimodal neural interfaces. *Science* **347**, 159–163 (2015).
56. Vachicouras, N. et al. Microstructured thin-film electrode technology enables proof of concept of scalable, soft auditory brainstem implants. *Sci. Transl. Med.* **11**, eaax9487 (2019).
57. Steinmetz, N. A. et al. Neuropixels 2.0: a miniaturized high-density probe for stable, long-term brain recordings. *Science* **372**, eabf4588 (2021).
58. Guan, S. et al. Elastocapillary self-assembled neurotassels for stable neural activity recordings. *Sci. Adv.* **5**, eaav2842 (2019).
59. Cea, C. et al. Enhancement-mode ion-based transistor as a comprehensive interface and real-time processing unit for in vivo electrophysiology. *Nat. Mater.* **19**, 679–686 (2020).
60. Lu, Chi et al. Flexible and stretchable nanowire-coated fibers for optoelectronic probing of spinal cord circuits. *Sci. Adv.* **3**, e1600955 (2017).
61. Li, L. et al. Integrated flexible chalcogenide glass photonic devices. *Nat. Photon.* **8**, 643–649 (2014).
62. Li, S., Su, Y. & Li, R. Splitting of the neutral mechanical plane depends on the length of the multi-layer structure of flexible electronics. *Proc. R. Soc. A* **472**, 20160087 (2016).
63. Kim, M.-G., Brown, D. K. & Brand, O. Nanofabrication for all-soft and high-density electronic devices based on liquid metal. *Nat. Commun.* **11**, 1002 (2020).
64. Morin, F., Chabanas, M., Courtecuisse, H. & Payan, Y. in *Biomechanics of Living Organs: Hyperelastic Constitutive Laws for Finite Element Modeling* (eds Payan, Y. & Ohayon, J.) 127–146 (Elsevier, 2017).

Methods

Materials and devices

Materials. Dow Sylgard 184 silicone encapsulant was used to prepare the PDMS thin films and was obtained from Corning. PIB (Exxon Butyl 268S) was obtained from Vanderbilt Chemicals. H-SEBS (Tuftec H1062) was obtained from Asahi Kasei. PI (PI2545 HD) was obtained from MicroSystems. PHFIPA and PPFHEA were prepared from hexafluoroisopropyl acrylate and 2-(perfluorohexyl)ethyl acrylate, respectively, which were obtained from Fluoryx Labs. PFPE-DMA with a molecular weight in the range 8,000–10,000 kg mol^{-1} was synthesized by Axoft, Inc. as reported previously[22,23]. Fluorolink MD700 was obtained from Solvay and was used as a crosslinker for PHFIPA and PPFHEA. 2-Hydroxy-2-methylpropiophenone was used as a photoinitiator.

Preparation of dielectric polymer thin films for characterization.
PFPE-DMA films. (1) Bis(2,4,6-trimethylbenzoyl)phenylphosphine oxide was used as photoinitiator, dissolved in bis(trifluoromethyl) benzene and mixed with PFPE-DMA, to prepare the photo-patternable precursor. (2) PFPE-DMA precursor was spin coated at 3,000 revolutions per min (r.p.m.). (3) The film was thermally dried for 2 min. (4) The film was exposed to UV light for a total dose above 150 mJ cm^{-2} under a nitrogen atmosphere.

SU-8 bilayer films. (1) SU-8 was spin coated at 3,000 r.p.m. (2) The film was baked at 65 °C for 2 min and at 95 °C for 2 min. (3) The film was exposed to UV light for a total dose above 150 mJ m^{-2} to completely cure the film and avoid pinholes. (4) The UV-cured film was post-baked at 65 °C for 2 min and at 95 °C for 2 min. (5) Defined patterns were developed using the SU-8 developer for 90 s, and then rinsed with isopropyl alcohol and blow-dried. (6) The developed patterns were hard-baked at 200 °C for 20 min. (7) Procedures (1)–(6) were repeated to define the second SU-8 layer to avoid pinholes.

PDMS (10:1) films. (1) PDMS base and curing agents (10:1 ratio) were mixed for 2 min and degassed for 2 min using a non-vacuum-type mixer (Thinky). (2) PDMS was spin coated at 5,000–8,000 r.p.m. (3) The PDMS films were baked at 65 °C overnight.

H-SEBS films. (1) H-SEBS was dissolved in toluene at 70–100 mg ml^{-1} and stirred for 48 h at 40 °C in a closed container. (2) The precursor solution was spin coated immediately at 1,000–2,000 r.p.m. after pouring it onto the substrate. (3) H-SEBS films were dried at 80 °C overnight.

PIB films. (1) Butyl 268S was dissolved in toluene at 10% of the solvent weight. (2) The precursor solution was spin coated immediately at 1,000–2,000 r.p.m. after pouring it onto the substrate. (3) PIB films were dried at 80 °C overnight.

PI films. (1) The precursor was spin coated at 3,000–4,000 r.p.m. immediately after pouring it onto the substrate. (2) Films were hard-baked using an atmosphere-controlled oven (vacuum purging, then under a continuous nitrogen flow) first at 200 °C for 30 min and then at 350 °C for 60 min.

PHFIPA and PPFHEA films. (1) The precursor was spin coated at 1,500 r.p.m. for 40 s. (2) Films were post-baked at 95 °C for 2 min. (3) Films were exposed to UV light for a total dose above 150 mJ m^{-2} to completely cure the film avoiding pinholes, under a nitrogen atmosphere. (4) Films were hard-baked at 110 °C for 1 h.

Fabrication of PFPE-DMA encapsulated neural probes. All photoresists and developers were obtained from Kayaku Advanced Materials unless otherwise mentioned. (1) A 100-nm-thick Ni sacrificial layer was patterned on the thermal oxide silicon wafer (University Wafer). (2) SU-8 2010 was patterned as spacers. (3) Cr/Au (15/100 nm) I/O pads were deposited via electron-beam evaporation. (4) For the bottom PFPE-DMA layer, the PFPE-DMA precursor was spin coated on the wafer at 2,000–6,000 r.p.m. to obtain a thickness ranging from 500 nm to 3 µm depending on the rotation speed and precursor concentration. The spin-coated PFPE-DMA film was aligned in a photomask aligner and patterned with UV light (10–30 mJ cm^{-2}) using a laboratory-made nitrogen diffuser (Extended Data Fig. 7b,c). Then the PFPE-DMA was post-baked at 115 °C, developed in bis(trifluoromethyl)benzene and blown dry. (5) For surface treatment, the PFPE-DMA surface was activated with inert gas plasma for 2–6 min. (6) For the metal interconnects, LOR3A and S1805 or S1813 photoresists were patterned on the wafer as described above. Different combinations of metal films, such as Al/Au, Al/Au/Al, Al/Au/Pt, Ti/Au, Ti/Au/Ti, Cr/Au and Cr/Au/Cr, were deposited by sputtering at Ar with a low oxygen atmosphere[65], with thicknesses in the range of 20–100 nm for each layer. Finally, the metal layers were lifted off using Remover PG solvent stripper overnight. (7) For multiple PFPE-DMA/metal layers, PFPE-DMA was spin coated and UV-cured, followed by plasma surface treatment, lift-off resist patterning and metal sputtering to create an additional layer of interconnects, similar to steps (4)–(6). Repeating this process multiple times will enable multilayer structures. (8) For the top PFPE-DMA layer, using the same recipe described in step (4), the top PFPE-DMA layer will be patterned. (9) For the SU-8 frame for transfer, SU-8 2010 was used to define a frame holding the soft brain probe during release. (10) The multilayer soft probes were released in nickel etchant (Transene), which is compatible with Al_2O_3- and Ti-based adhesion layers.

Electroplating of electrodes. We used an SP-150e potentiostat (Bio-Logic) along with its commercial software EC-lab V11.36 (https://www.biologic.net/support-software/ec-lab-software/) for electrodeposition. Electrodes from neural probes were connected to the working electrode. A platinum wire immersed in the precursor solution was used as the counter electrode, which also serves as the voltage reference. For the deposition of Pt black, the precursor solution consisted of 1 mM chloroplatinic acid solution and 25 mM sodium nitrate. Cyclic voltammetry with a potential varying from −1.0 V to 0.2 V at 0.05 V s^{-1} for 10–15 cycles was used. For PEDOT:PSS deposition, an electrolyte consisting of 0.01 M 3,4-ethylenedioxythiophene (Sigma-Aldrich) and 0.1 M poly(4-styrenesulfonic acid) sodium salt (Sigma-Aldrich) aqueous solution was used. The electrochemically polymerized reaction was performed under constant-voltage conditions. In the constant-voltage mode, the polymerization was carried out under a constant current of 1 V for 30 s.

Characterization

Thickness measurements. All thickness measurements were carried out using a DektakXT stylus profiler (Bruker). The force applied was set to 1 mg and the scan speed was 0.67 µm s^{-1}. Two-point surface levelling was applied using the commercial software of the tool.

Characterization of mechanical properties. Stress–strain curves and fracture toughness measurements were obtained using a testing machine (Instron) in uniaxial tension for specimens in the pure shear test geometry. A 90° peeling test was used to determine the adhesion energies.

Characterization of electrical properties. Current–voltage (I–V) curves for the metal interconnects on the PFPE-DMA substrates were measured using a probe station connected to an Axon Digidata 1550B plus HumSilencer to output controlled voltages. Input currents were amplified using a current pre-amplifier before measurement by the data acquisition card.

Characterization of surface properties. The contact angles of LOR3A and DI water on PFPE-DMA were determined using the free DropSnake plugin on ImageJ[65].

EIS measurements. The three-electrode setup used was the same as reported in our previous work[37]. For each measurement, three sweeps in frequency were measured, from 1 MHz down to 0.1 Hz. A sinusoidal voltage of 100 mV peak-to-peak was applied. Five points per frequency decade, logarithmically spaced, were measured. For each data point, the response to ten consecutive sinusoids (but spaced out by 10% of the period duration) was accumulated and averaged.

EEC measurements. A Traceable Conductivity Pocket Tester with Calibration was used to measure the conductance of the solutions. The two electrodes have an area of 1 cm^2 and are separated by 1 cm. The resolution of the sensor was 1 µS, and the temperature dependence of the conductance in the range of −5 to 50 °C was automatically compensated to give the value at 25 °C.

SEM and FIB imaging. A metal sputter coater was used to deposit a 20-nm-thick Pt/Pd layer and reduce the charging under the electron beam during the SEM imaging process. SEM images were taken under 5 kV voltage using a JEOL 7900F SEM instrument. Before FIB milling, another 100-nm-thick layer or Pt was deposited using the metal sputter coater atop the sample to prevent damage of the area of interest under ion beams. The FIB process followed conventional procedures using an FEI Helios 660 instrument in which a 30 kV Ga beam was used for rough milling and a reduced 10 kV voltage was used for fine milling. To inspect the sample surface of the FIB-milled cross-section, a secondary electron detector under 3 kV voltage was used to take the SEM images, which showed clear contrast and distinct layering out of the samples.

Animal experiments

Brain and spinal cord implantation. All animal experiments in this study were approved by the Institutional Animal Care and Use Committee of Harvard University under protocols 19-03-348 and 20-05-368. The implantations were carried out on male C57BJ/6 mice (25–35 g; 6–8 weeks of age), which were housed in a regular 12 h/12 h light/dark cycle. The animals were anaesthetized with 2–3% isoflurane and maintained under anaesthesia with 0.75–1% isoflurane during the implantation surgery. Two stainless-steel screws were implanted in the cerebellum and used as ground electrodes. A craniotomy was performed on the brain, and the cortical surface was exposed upon removal of the dura mater. The PFPE-DMA brain probe was placed on the surface of the cortex and inserted using a 75 µm tungsten wire anchored to the neural probe through a fabricated hole at the front end of the device. For histological studies, SU-8 devices of the same size were implanted contralaterally in mouse brains for comparison. For spinal cord implantation, PFPE-DMA and 25-µm-thick PI probes were implanted in the mice through the following steps. First, the mice were anaesthetized, placed on a heating pad and given a midline incision on their vertebrae to expose the spinal cord. Then, an approximately 1 × 1 mm window was drilled on the L2–L3 lumbar vertebrae and the dura mater was removed to expose the tissue. Next, PFPE-DMA and PI probes were inserted into the subdural space of the L2–L3 segments in mice. Finally, a group of mice that received spinal cord surgery without probe implantation was used as sham controls.

Electrophysiological recordings. For data acquisition, a Blackrock Microsystems CerePlex µ headstage was connected to the flat flexible cable on the head of the mice through a laboratory-made printed circuit board. We used a CerePlex Direct data acquisition card and the CerePlex software to record and filter the electrophysiological recordings. The electrophysiological recording data were analysed offline. In brief, raw recording data were filtered using a bandpass filter in the 300–3,000 Hz frequency range. Spike sorting was performed using Mountainsort 4 software (https://github.com/flatironinstitute/mountainsort). The amplitude for each recording channel was calculated by the peak-to-peak amplitude of all sorted spikes. The spiking times of each cluster (that is, each single unit) were used to compute the ISI histogram. Recordings of electrical activity from the spinal cord using chronically implanted PFPE-DMA neural probes were performed after between six and eight weeks of implantation. For the spike-like electrical activity, a 250–3,000 Hz frequency range filter was applied to the voltage signals in the CerePlex software, and a threshold detection at −5 s.d. PCA was used for dimension reduction and MATLAB's 'kmeans' function was used to cluster the extruded waveforms.

Immunostaining. Brain tissue. Immunohistochemistry and confocal fluorescence imaging were performed according to our previous reports[11,66]. (1) Mice were anaesthetized with 40–50 mg per kg (body weight) sodium pentobarbital and then transcardially perfused with 1x PBS (40 ml) and 4% paraformaldehyde (40 ml) followed by decapitation. (2) The brains implanted with SU-8/PFPE-DMA probes were removed from the cranium and post-fixed in paraformaldehyde for 24 h at 4 °C. (3) The samples were transferred to sucrose solutions with a stepwise increase in concentration from 10% to 30% (w/v) until they sunk to the bottom. (4) The samples were embedded in optimal cutting temperature compound and cut into 30-µm-thick slices using a cryostat. Brains implanted with SU-8 brain probes with the same thickness were used as controls. (5) The brain slices were first incubated with primary antibodies (NeuN: 1:200 (ab177487, Abcam); GFAP: 1:200 (ab4674, Abcam or 3670, Cell Signaling Technology); IBA1: 1:100, (ab5076, Abcam or 17198, Cell Signaling Technology)) at 4 °C overnight. After washing with 1x PBS three times, the brain slices were incubated with secondary antibodies at room temperature for 3–4 h. (6) The brain slices were stained with 4′,6-diamidino-2-phenylindole (DAPI) for 10 min. (7) After washing with 1x PBS, all samples were imaged with a Leica TCS SP8 confocal microscope using the Leica Application Suite X software platform 3.5.5 (https://www.leica-microsystems.com/products/microscope-software/p/leica-las-x-ls/downloads/).

Spinal cord tissue. (1) At six weeks post-implantation, mice were anaesthetized with 40–50 mg per kg (body weight) sodium pentobarbital and then transcardially perfused with 1x PBS (40 ml) and 4% paraformaldehyde (40 ml) followed by decapitation. (2) The spinal cord tissues were removed and post-fixed in paraformaldehyde for 24 h at 4 °C. (3) The fixed tissue samples were transferred to sucrose solutions with a stepwise increase in concentration from 10% to 30% (w/v) until they sunk to the bottom. (4) The samples were embedded in optimal cutting temperature compound and cut into 30-µm-thick slices using a cryostat. Spinal cords implanted with 25-µm-thick PI probes were used as controls, and a group of mice that received spinal cord surgery without implants was used as sham controls. (5) The spinal cord slices were incubated with primary antibodies (GFAP: 1:200 (ab4674, Abcam) and IBA1: 1:100 (ab5076, Abcam)) at 4 °C overnight. After washing with 1x PBS three times, the slices were incubated with secondary antibodies at room temperature for 3–4 h. (6) The spinal cord slices were stained with DAPI for 10 min. (7) After washing with 1x PBS, all samples were imaged with a Leica TCS SP8 confocal microscope using the Leica Application Suite X software platform 3.5.5.

Open-field testing. To perform the open-field analysis, we used a 40 × 40 × 40 cm (length × width × height) open arena. All animals were tested during their more active dark cycle in a sound-attenuated laboratory maintained at 23 °C. The animals were placed in the centre of the arena and allowed to freely explore the open-field enclosure for 10 min while being recorded with an overhead camera. Digital recordings were collected, and the central positions of the animals were labelled using the DeepLabCut (DLC) toolbox (https://github.com/DeepLabCut/DeepLabCut) for the motion analysis. The animals' movements were defined as periods when the velocity of the animals' centre point

averaged more than 2 cm s^{-1}. The distance travelled and average speed were calculated from the 10 min recording.

Gait analysis. The behaviour setup for the ladder-rung test involved using a GoPro 11 camera at 240 frames per second to record the mice consecutively running on a custom-made ladder. In this test, the animals crossed horizontal ladders while their footfalls were being recorded. Animals were habituated to a ladder with regularly spaced rungs before any experiments were performed. We used DLC to label the hind paws and detect the footfall using a peak detection algorithm, with video verification by the researchers. We also used DLC to perform limb tracking of six hindlimb joints (toe, metatarsophalangeal joint, ankle, knee, hip and iliac crest) for kinematic analysis of the hindlimb trajectories.

Simulations

Molecular dynamics simulations. (1) Low-density polymer matrices (~60–70% of the equilibrium density of each polymer at 300 K) were generated with five water molecules or five NaCl molecules added as solutes. Each simulated polymer was simulated by 100 monomers per chain and 15 chains per simulation box. The full breakdown of the number of atoms per polymer architecture is summarized in Supplementary Table 1. (2) The Maestro Suite of Schrödinger LLC[67] was used to pack the polymer chains and water/NaCl molecules into a simulation box. The force field used to describe the potential energy of the systems is OPLS[68], as developed and optimized by Schrödinger. For every polymer–solute combination, five independently generated structures were created with the goal to better sample the phase space of the polymer and to obtain ensemble averages and uncertainties. (3) The MD simulations were run using the Desmond MD code[69]. A time step of 1 fs was used to evolve the equations of motion. Once generated, the structures were brought close to equilibrium at 300 K through a set of MD stages described in Supplementary Table 2. (4) At the end of the equilibration, a canonical simulation of 2 ns was run to determine the density of the polymer at 300 K. (5) To determine the diffusion, a simulation of 250 ns was run in the canonical ensemble. The positions of all atoms/molecules of interest were tracked and the mean squared displacement (MSD) was computed. The MSD versus time curve was then post-processed to detect linear regions with a slope (in the log–log plot) equal to unity (that is, corresponding to the diffusive regime). This protocol was repeated for all polymer structures at a different temperature to construct the Arrhenius plot for all polymers investigated.

Finite element analysis. Abaqus 6.12 was used to analyse the mechanical properties of different polymer probes. The goal of the simulations is to evaluate the strain and stress concentration of composite beams bending around a capillary of circular cross-sections under gravity. The probes are made of three layers: a 140-nm-thick central metal layer between two 4.5-μm-thick dielectric layers with the elastic modulus of PFPE-DMA or SU-8. The elements used are S4R5 or S4R, with a mesh size of 50 μm, and a contact between the probes and the capillary modelled by surface-to-surface normal forces only (shear-free contact).

Statistics and reproducibility

The results of the micrographs in Fig. 3c–e have been repeated independently for more than three wafers. The devices shown in Extended Data Fig. 6n–t were reproduced more than six times. The micrographic areas shown in Extended Data Fig. 7j,k have been captured for >32 interconnects. The results shown in Extended Data Fig. 8h–k,m–o have been repeated more than three times for each of the panels.

Reporting summary

Further information on research design is available in the Nature Portfolio Reporting Summary linked to this article.

Data availability

All data and materials that supporting the findings of this study are available within the paper and its Supplementary Information. Source data are provided with this paper.

Code availability

The authors declare that all the code supporting the findings of this study are available within the paper and its Supplementary Information. DeepLabCut is available at https://github.com/DeepLabCut/DeepLabCut. Mountainsort 4 is available at https://github.com/flatironinstitute/mountainsort. DropSnake is available at https://bigwww.epfl.ch/demo/dropanalysis/.

References

65. Stalder, A. F., Kulik, G., Sage, D., Barbieri, L. & Hoffmann, P. A snake-based approach to accurate determination of both contact points and contact angles. *Colloids Surf. A* **286**, 92–103 (2006).
66. Zhao, S. et al. Graphene encapsulated copper microwires as highly MRI compatible neural electrodes. *Nano Lett.* **16**, 7731–7738 (2016).
67. Schrödinger Release 2021-2: Maestro (Schrödinger Inc., 2021).
68. Harder, E. et al. OPLS3: a force field providing broad coverage of drug-like small molecules and proteins. *J. Chem. Theory Comput.* **12**, 281–296 (2016).
69. Bowers, K. J. et al. Scalable algorithms for molecular dynamics simulations on commodity clusters. In *SC '06: Proc. 2006 ACM/IEEE Conference on Supercomputing* 43 (IEEE, 2006).

Acknowledgements

We acknowledge the discussion and assistance from all Liu Group members. We acknowledge the support from NSF through the Harvard University Materials Research Science and Engineering Center Grant No. DMR-2011754; the Harvard University Center for Nanoscale Systems supported by the NSF; and the Aramont Fund for Emerging Science Research.

Author contributions

P.L.F., S.Z., R.L. and J. Liu designed the experiments. P.L.F., H. Sheng, G.Z., C.S., W.W., X.W. and A.S. synthesized the fluorinated polymers. P.L.F. characterized the dielectric stability of polymer thin films. N.M. and B.K. conducted the MD simulations. P.L.F., R.L., H. Sheng, H.P. and X.G. developed the nanofabrication process for the neural probes. P.L.F., T.Y., J. Lee, X.G. and R.L. characterized the electrical properties of the neural probes. R.L. performed the SEM and FIB characterization. P.L.F. and S.Z. performed the animal experiments. P.L.F., S.P., H. Shen and X.T. analysed the electrophysiological recordings from behaving animals. J.K., Z.W., N.L. and Z.S. simulated and characterized the mechanical properties of the materials and devices. E.M. and K.B. conducted the finite element analysis. P.L.F. and J. Liu wrote the manuscript. All authors discussed and commented on the manuscript. J. Liu supervised the project.

Competing interests

P.L.F., H. Sheng and J. Liu are on a patent application filed by Harvard University related to this work. P.L.F., H.P., X.G., A.S., J. Lee, T.Y. and J. Liu declare financial interests in Axoft, Inc. The other authors declare no competing interests.

Additional information

Extended data is available for this paper at https://doi.org/10.1038/s41565-023-01545-6.

Supplementary information The online version contains supplementary material available at https://doi.org/10.1038/s41565-023-01545-6.

Correspondence and requests for materials should be addressed to Jia Liu.

Peer review information *Nature Nanotechnology* thanks the anonymous reviewers for their contribution to the peer review of this work.

https://doi.org/10.1038/s41565-023-01545-6

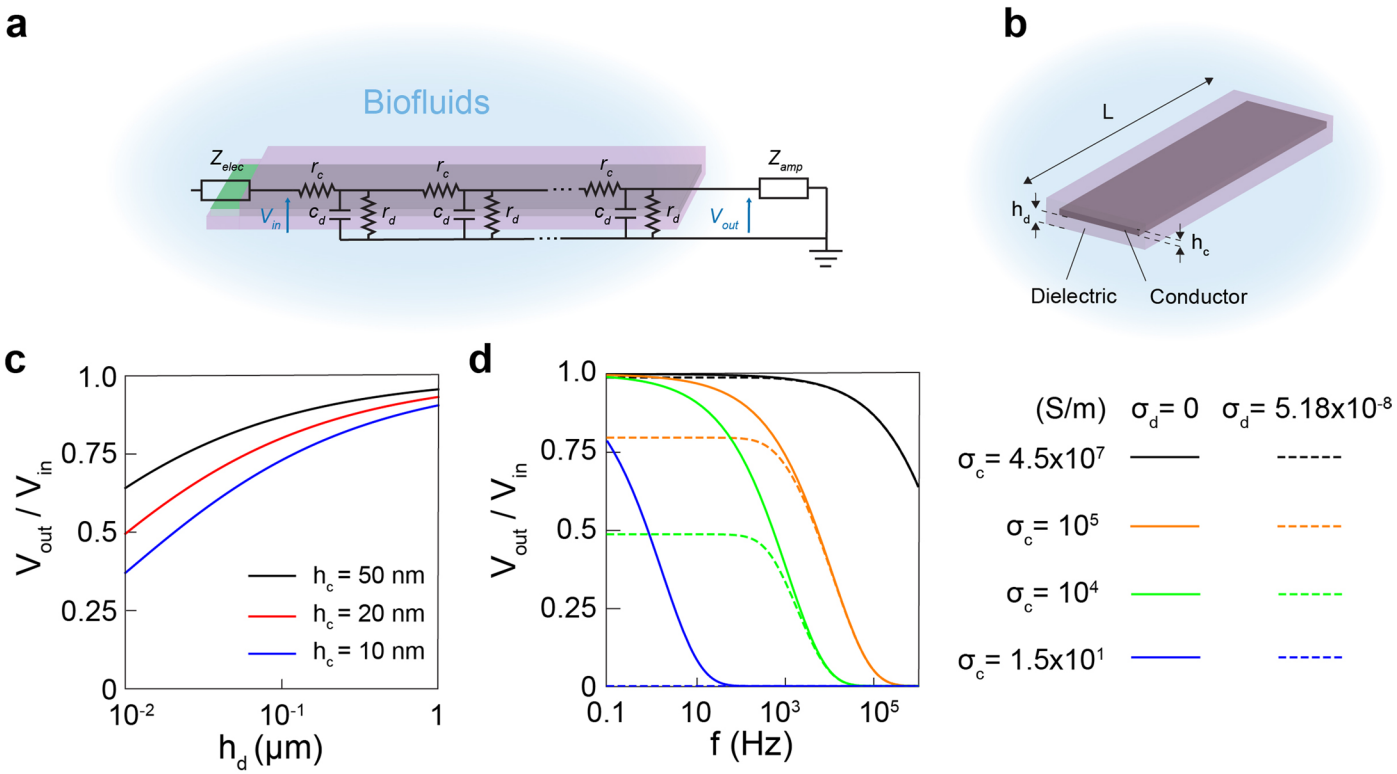

Extended Data Fig. 1 | Modeling of electrical insulation performances of thin-film dielectrics in electrodes. a, Schematic showing the transmission line model with conductive losses through the thin film dielectric encapsulation in a representative microelectrode structure. V_{in}, V_{out}, Z_{elec}, Z_{amp}, r_c, c_d, and r_d denote the input voltage at the electrode tip, the output voltage, the electrode tip electrochemical impedance, the amplifier's input impedance, the sheet resistance of the conductive line, the capacitance per unit length of the dielectric, and the resistance per unit length of the dielectric, respectively. **b**, Stripline geometry for the electrode interconnect line insulated by a dielectric. L, h_c, and h_d denote the length of the electrode, the thickness of the conductor, and the thickness of dielectric encapsulation on each side, respectively. **c**, Signal attenuation at 10 kHz plotted as a function of h_d (for a dielectric constant $\varepsilon_d = 3.2$) for various thicknesses h_c of the metal line (with a conductivity $\sigma_c = 4.5\times10^7$ S/m). **d**, Signal attenuation as a function of frequency for various values of σ_c at the lossless ($\sigma_d = 0$) condition or lossy condition ($\sigma_d = 5.18\times10^{-8}$ S/m) due to ionic conduction within the dielectric encapsulation[37]. $L = 0.05$ m in (**c**) and (**d**), $h_c = 50$ nm and $h_d = 1$ μm in (**c**).

https://doi.org/10.1038/s41565-023-01545-6

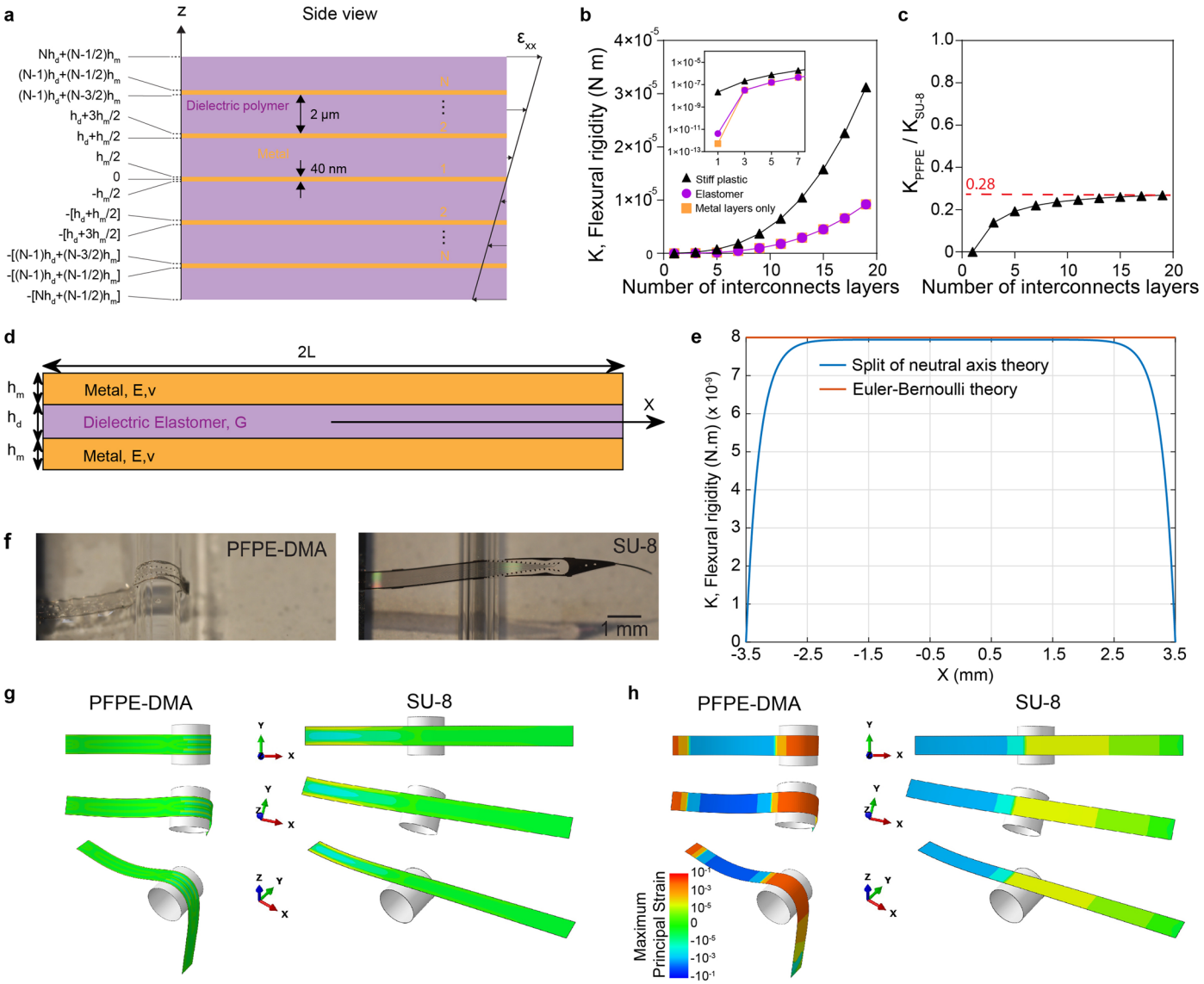

Extended Data Fig. 2 | Composite beam model of scalable neural probes. **a**, Composite beam model of a neural probe with 2N-1 layers of metal interconnects. h_d and h_m respectively denote the dielectric encapsulation and metal layer thickness. **b**, Flexural rigidity in the composite beam model of (**a**) as a function of the number of metal layers. This is the same simulation as used in Fig. 1g. **c**, Elastomer-to-plastic neural probes' flexural rigidity ratio as a function of the number of metal layers. We choose $E_{plastic}$ = 4 GPa, $\nu_{plastic}$ = 0.33, $E_{elastomer}$ = 0.5 MPa, $\nu_{elastomer}$ = 0.5, E_{metal} = 79 GPa, ν_{metal} = 0.22, h_d = 2 μm and h_m = 40 nm. **(d, e)** *X*-dependent flexural rigidity considering the split of neutral axis due to extreme modulus mismatch between metal and elastomer layer**.** **d**, Schematic for the trilayer beam bending problem. **e**, Flexural rigidity in the majority of the probe away from the free ends approaches the Euler-Bernoulli prediction. **(f-h)** Comparison of the mechanical behavior of soft PFPE-DMA and stiff SU-8 neural probes. **f**, Bending of 9-μm-thick, 500-μm-wide PFPE-DMA (left) and SU-8 (right) neural probes with a 140-nm-thick central Au layer, around a 1-mm-diameter glass capillary. (**g, h**) Finite element analysis of the bending of PFPE-DMA (left) and SU-8 (right) neural probes with the same geometry as in (**f**). The maximum principal strain is represented in the central metal layer (**g**) and the upper dielectric layer (**h**).

https://doi.org/10.1038/s41565-023-01545-6

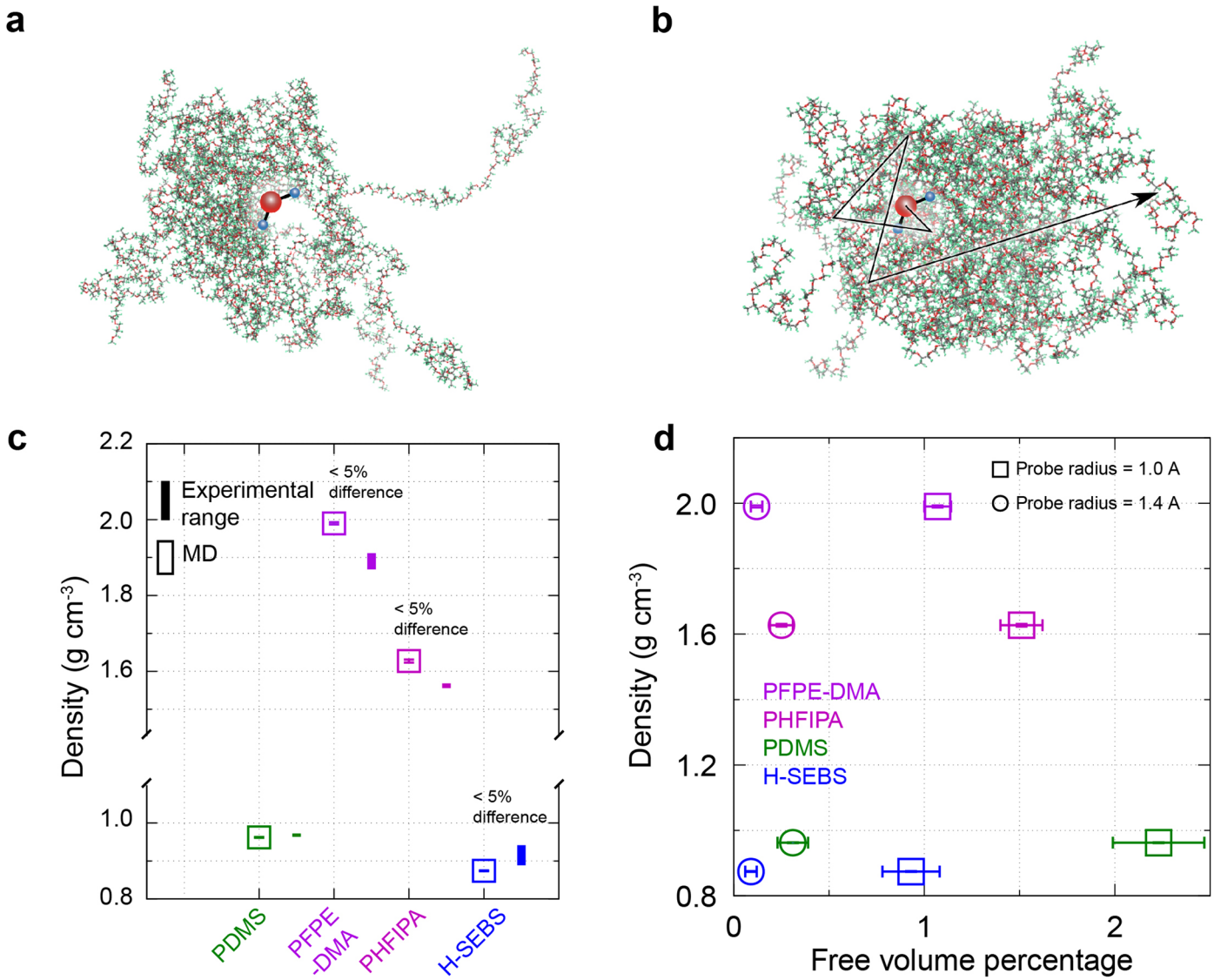

Extended Data Fig. 3 | MD simulations. (**a, b**) Simulated PFPE-DMA polymer chains before (**a**) and after (**b**) equilibration. The structure contains a water molecule enlarged for visibility. Black arrow is a cartoon view depicting the diffusion of the molecule during the simulation. **c**, Comparison of polymer densities obtained by MD simulation to data from the literature. **d**, Free volume percentage versus density of polymers obtained by MD simulations. Value = mean ± S.D. and $n = 5$ for each material in panels (**c**) and (**d**).

https://doi.org/10.1038/s41565-023-01545-6

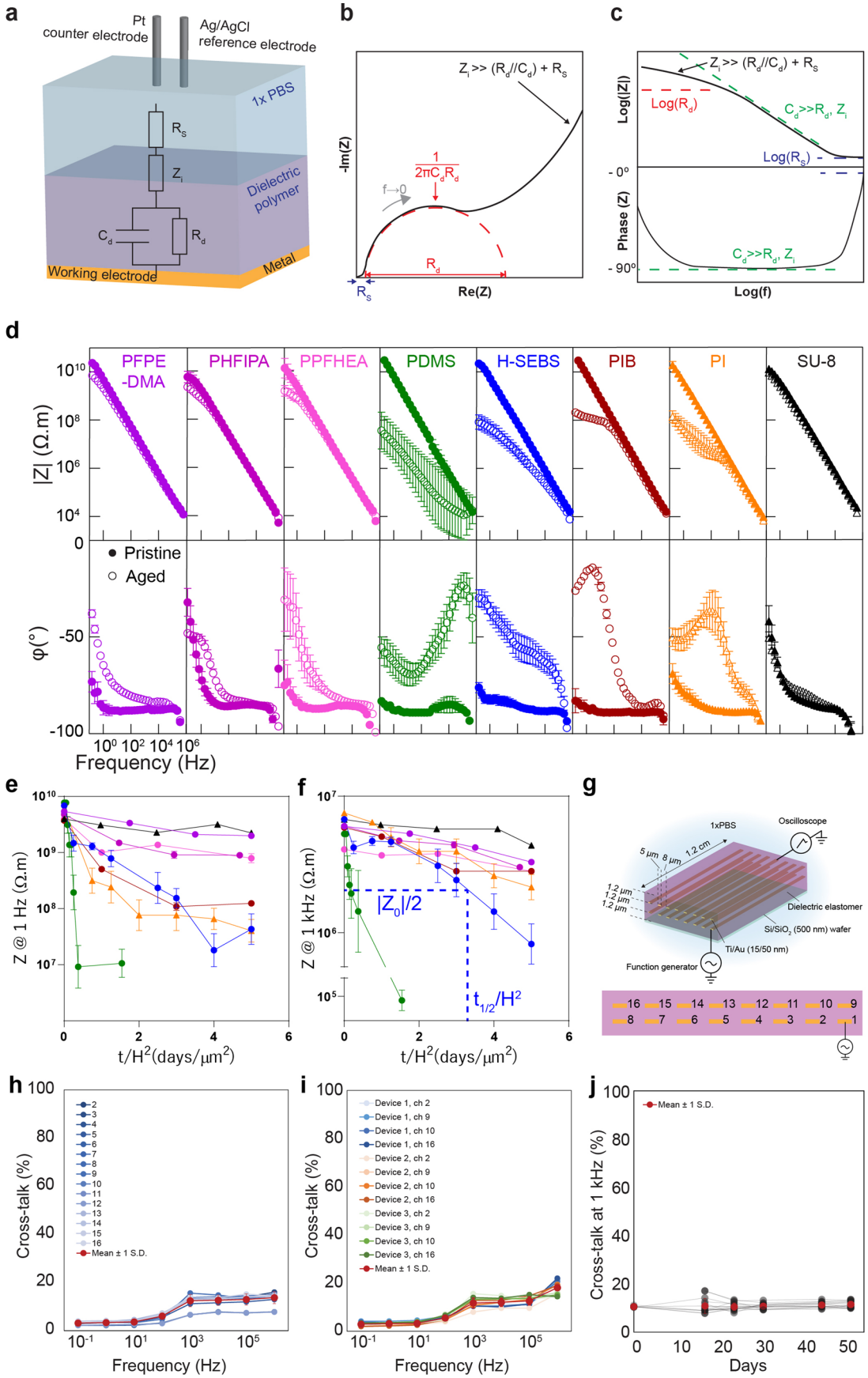

Extended Data Fig. 4 | See next page for caption.

https://doi.org/10.1038/s41565-023-01545-6

Extended Data Fig. 4 | Electrochemical impedance spectroscopy (EIS) of dielectric polymer thin film and crosstalk between encapsulated microelectrodes in physiological solution over time. a, Schematic showing the equivalent circuits of the dielectric polymer film in the three electrodes setup during EIS. R_s and Z_i represent the electrolyte resistance and interfacial impedance between the electrolyte and dielectric polymer, respectively. C_d and R_d represent the capacitance and resistance (due to the built-in ionic conductivity) of the dielectric polymer film, respectively. **b**, Schematic of a typical Nyquist plot of the electrochemical impedance measured in (**a**) adapted from Bard *et al.*[41] As the thickness of the dielectric layer defines C_d, R_d can be extracted by fitting the Nyquist plot to a semi-circle at high frequencies[37]. **c**, Schematic of a typical Bode plot of the electrochemical impedance in (**a**). At low frequencies, deviation from the purely capacitive behavior of the dielectric polymer can be observed due to the built-in ionic conductivity. **d**, Averaged Bode plots (value = mean ± S.D., n = 4, 4, 4, 8, 12, 4, 3, 4 samples for PFPE-DMA, PHFIPA, PPFHEA, PDMS, H-SEBS, PIB, PI, SU-8, respectively) of modulus (top) and phase (bottom) of the normalized electrochemical impedance of dielectric polymers in their pristine condition and after aging in 10x PBS at 70 °C (at t/H^2 = 5 days/μm^2 for PFPE-DMA, PHFIPA, PPFHEA, PDMS, H-SEBS, PI, SU-8 and t/H^2 = 1.55 days/μm^2 for PDMS*). (**e, f**), Modulus of the normalized electrochemical impedance of various dielectric elastomers at 1 Hz (**e**) and 1 kHz (**f**) as a function of the normalized soaking time by the square of the sample thickness in 10x PBS at 70 °C (value = mean ± s.e.m., n = 4, 4, 4, 8, 12, 4, 3, 4 samples for PFPE-DMA, PHFIPA, PPFHEA, PDMS, H-SEBS, PIB, PI, SU-8, respectively). In (**f**), $t_{1/2}/H^2$ corresponds to the time required to decrease the initial modulus of the normalized impedance (Z_0) by 50%. *PDMS samples degradation is very fast and debonding from the working electrode occurred around t/H^2 = 2 days/μm^2. Therefore, experiments for PDMS characterization were stopped before reaching t/H^2 = 5 days/μm^2. The vertical scale break is used to plot the lowest point in the PDMS curve. **g**, Schematics of the device used for the crosstalk test. The device consists of an array of 16 conductive metal interconnects regularly spaced over two layers and encapsulated by 1.2-μm-thick PFPE-DMA layers. The test devices are immersed in a grounded 1x PBS solution during measurement. **h**, Crosstalk measured as a function of frequency between channel 1 and the 15 other interconnects of the array (n = 15 interconnects). **i**, Crosstalk measured as a function of frequency for four interconnects located at the same position for three different samples (n = 4 for each device). **j**, Crosstalk at 1 kHz for a given sample (n = 15 interconnects) plotted as a function of soaking time in 1x PBS.

https://doi.org/10.1038/s41565-023-01545-6

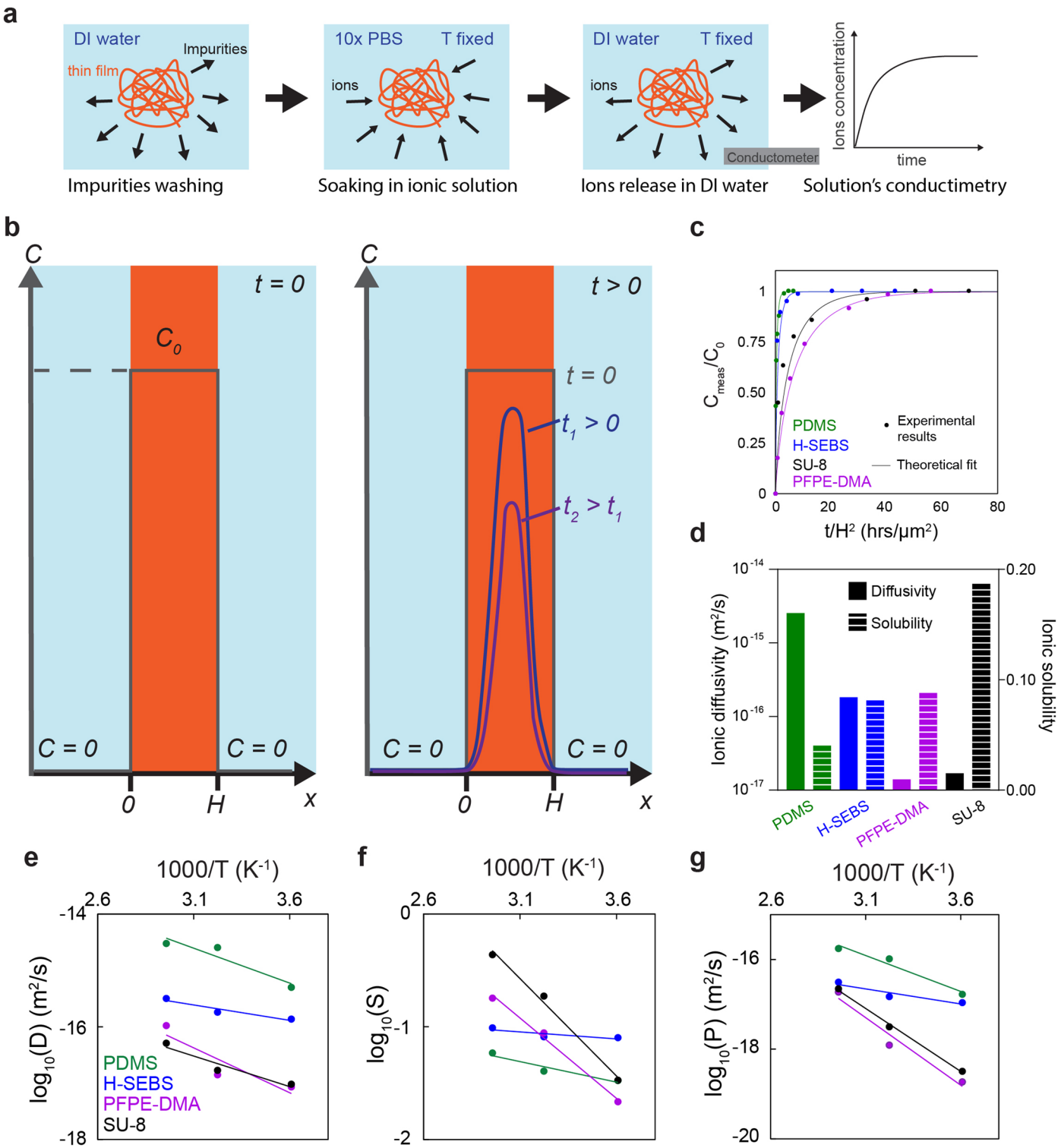

Extended Data Fig. 5 | External Electrolyte Conductimetry (EEC) of dielectric polymer thin film. a, Schematics of the experimental design. **b**, Schematics of equivalent boundary value problem and results for the diffusion of ions during EEC measurement. The schematics show ionic concentration inside the ion-filled polymer thin film over time of soaking in DI water. C_0 represents the initial concentration of ions in the polymer thin film, and C is the concentration of ions in the DI water. **c**, Fitting of the experimental results to obtain ionic diffusivity D. **d**, Estimation of ionic diffusivity, D, and solubility, S, obtained by EEC for dielectric polymer thin films. **(e-g)** Temperature dependence of ionic diffusivity, solubility, and permeability of polymer thin films characterized by EEC measurement. **e**, Logarithm of the ionic diffusivity, D, measured by the EEC measurement, as a function of 1000/T (K^{-1}). **f**, Logarithm of the ionic solubility, S, measured by EEC measurement, as a function of $1000/T$ (K^{-1}). **g**, Logarithm of the ionic permeability, P, defined as the product $S*D$ as a function of 1000/T (K^{-1}). The linear fits in (**e-g**) were used to obtain energy parameters in Supplementary Table 7. T is the temperature for (**e-g**).

https://doi.org/10.1038/s41565-023-01545-6

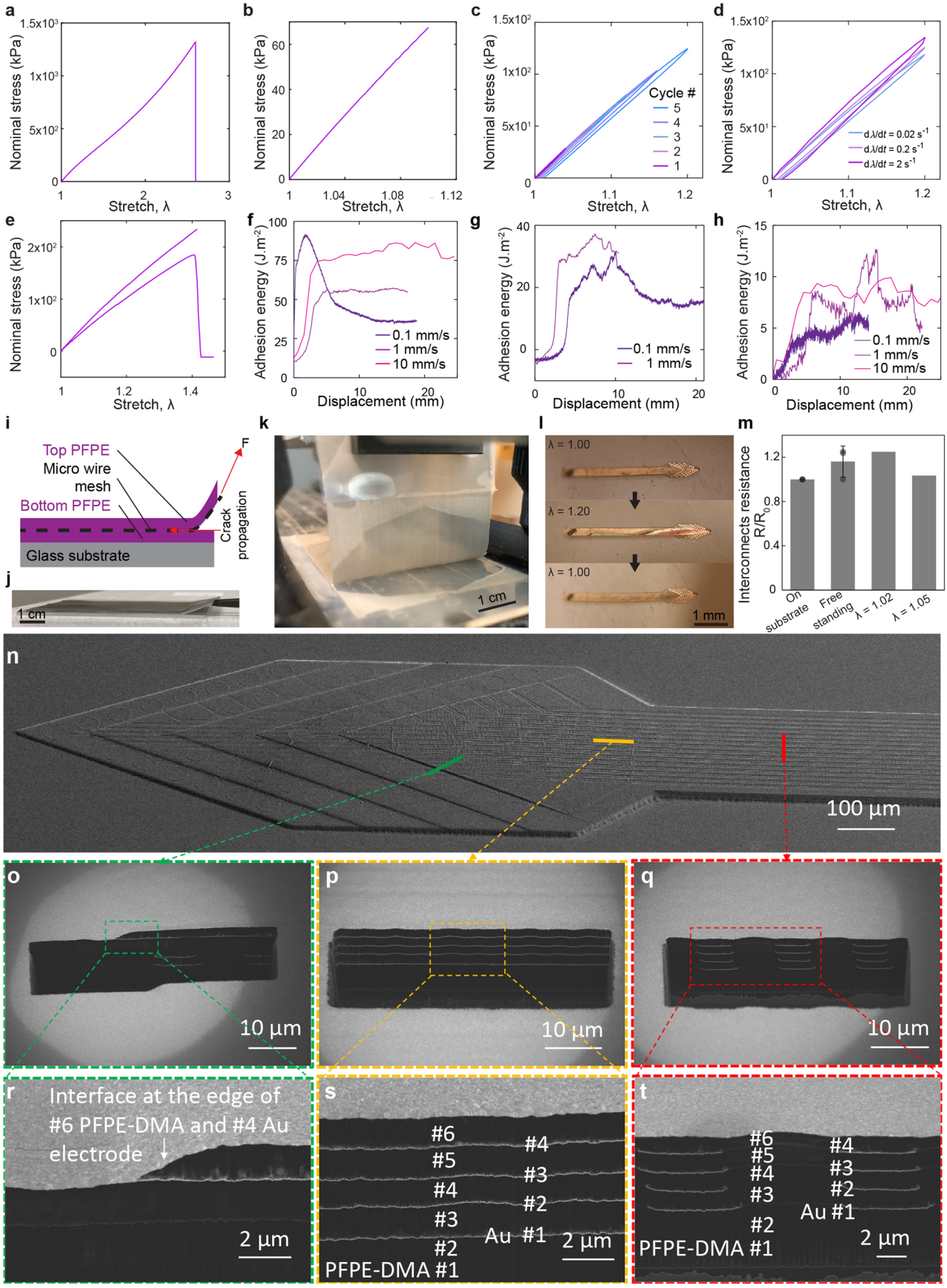

Extended Data Fig. 6 | See next page for caption.

https://doi.org/10.1038/s41565-023-01545-6

Extended Data Fig. 6 | Mechanical testing of PFPE-DMA films under various conditions. (**a**-**e**) Tensile testing of PFPE-DMA films. **a**, Stress-stretch curve in uniaxial tension to rupture. The data are from Fig. 2h. **b**, Stress-stretch curve in uniaxial tension, with a maximum stretch of 1.1 to determine the elastic modulus (strain rate of 0.2 s^{-1}). **c**, Cyclic testing with a progressive increase in the maximum stretch. **d**, Cyclic testing with a progressive increase in strain rate to show the rate-dependency of the hysteresis. **e**, Pure shear test of two specimens with a pre-crack to determine fracture toughness. We estimate a fracture toughness of 128 and 261 J/m^2 for each specimen. **(f-k)** Adhesion energy measurements between PFPE-DMA layers. (**f, g**) PFPE-DMA – PFPE-DMA adhesion energies measured with the 90° peel test for two samples (using a stainless-steel microwire mesh in (**f**) and a Nylon mesh in (**g**)) as a function of displacement. As the displacement first increases, the crack blunts but does not grow, and the force increases (thus the energy measured) until the crack starts to propagate. The plateau characterizes the adhesion energy. Higher peeling rates correspond to higher adhesion energy values, due to the viscoelasticity of PFPE-DMA. **h**, PFPE-DMA – glass adhesion energy is lower than PFPE-DMA - PFPE-DMA adhesion energy in (**f, g**). **i**, Schematic of the 90° peel test. A microwire mesh (stainless steel or Nylon) lays on top of the first layer of PFPE-DMA solvent cast and hard-baked on a glass slide. The second layer of PFPE-DMA, thicker than the microwire mesh, is solvent casted and hard-baked on top of the mesh. Polyimide tape prevents the adhesion of the microwire mesh to the bottom layer of PFPE-DMA on one side, to initiate the pre-crack. **j**, Photograph of a sample, tweezers show the side with the polyimide tape for the pre-crack. **k**, Photograph taken during the 90° peel test. **l**, Delamination-free large deformation of multilayer PFPE-DMA neural probes. Photograph of a 4-metal layer PFPE-DMA neural probe on a thick, stretchable H-SEBS substrate before, during, and after uniaxial stretching. **m**, Resistance of metal interconnects in PFPE-DMA neural probes before and after uniaxial stretch. Relative changes in the resistance of the metal interconnects before ($n = 3$ interconnects) and after ($n = 3$ interconnects) releasing the device from the fabrication substrate and applied 2% ($n = 1$ sample) and 5% ($n = 1$ sample) uniaxial stretch (value = mean ± S.D. when $n > 1$ samples). (**n**-**t**) SEM images of a multilayer soft neural probe after undergoing an accelerated aging test in 1x PBS at 65 °C for 10 days. SEM overview of the probe (**n**) with three FIB-cut positions labeled in green, orange, and red, corresponding to cross-sections along the interconnect direction at the interface of electrode and interconnect (**o, r**), (**p, s**) parallel to the interconnects, (**q, t**) perpendicular to the interconnects.

https://doi.org/10.1038/s41565-023-01545-6

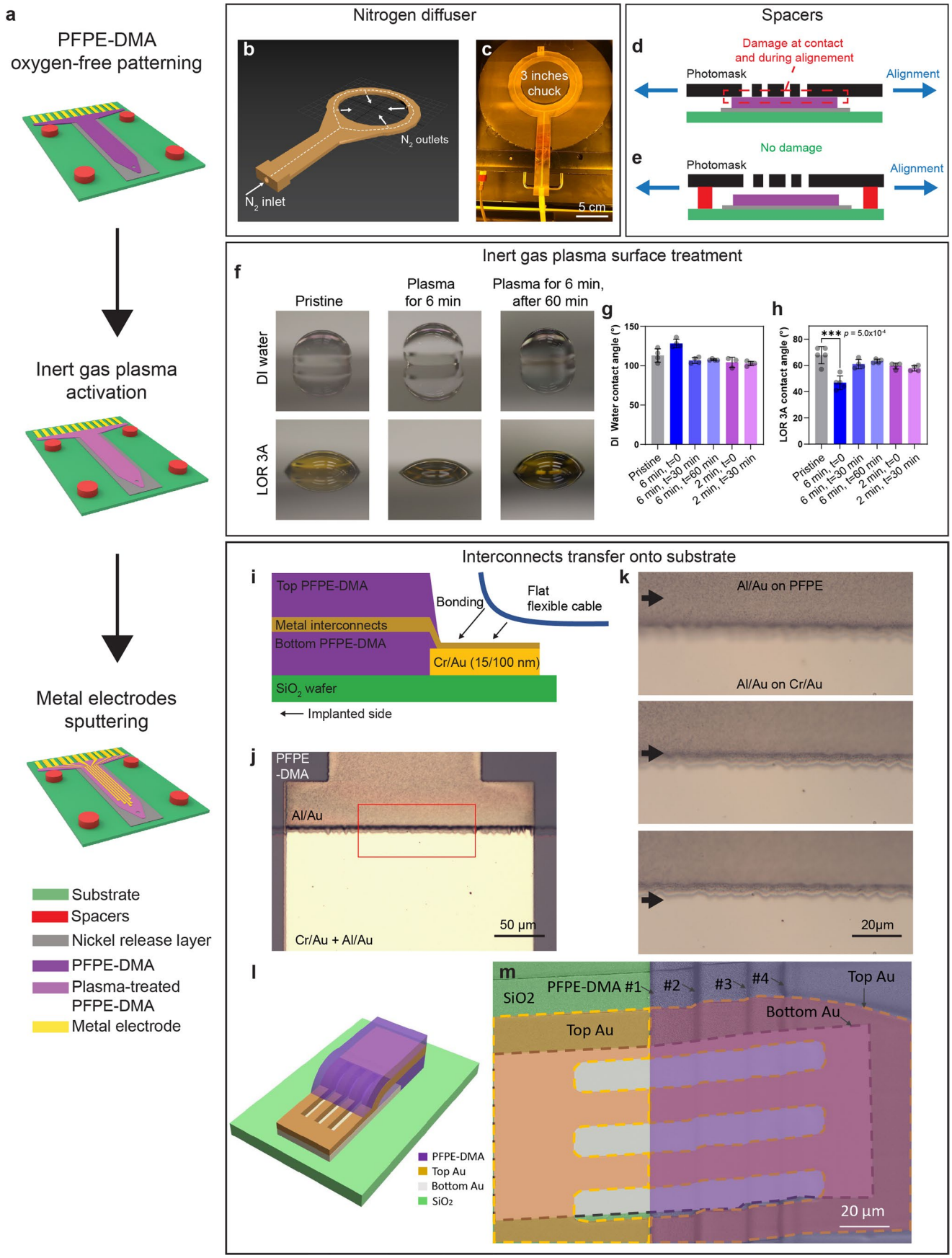

Extended Data Fig. 7 | See next page for caption.

https://doi.org/10.1038/s41565-023-01545-6

Extended Data Fig. 7 | Nanofabrication of soft neural probes. a, Schematics showing the stepwise nanofabrication process of 3D stacked soft electrode arrays encapsulated by PFPE-DMA elastomers. (**b, c**) Schematic design (**b**) and photographic image (**c**) showing the photomask aligner-compatible, 3D-printed Nitrogen diffuser that provides the Nitrogen atmosphere for an oxygen-free photolithography. The Nitrogen diffuser is compatible with the standard 3-inch chuck of a Karl Suss MA6 mask aligner. **(d, e)** Schematics show the side views of the fabrication substrate inside a photomask aligner without (**d**) or with (**e**) a photolithographically defined SU-8 spacer. Without the SU-8 spacer, the direct contact to the photomask damages the soft fluorinated elastomer precursor spin-coated onto the substrate (**a**). In contrast, with the spacer, the few micrometers gap between the PFPE-DMA surface and the photomask preserves the integrity and smooth surface of PFPE-DMA film, allowing for high-resolution patterning required for the soft brain probes fabrication. **(f-h)** Enabling photolithographic patterning of metals by plasma treatment of PFPE-DMA films. **f**, Photograph of DI water (top) and LOR 3 A (bottom) drops on the PFPE-DMA film surfaces in their pristine state, immediately after 6 min plasma treatment, and 1 hr in ambient condition after the plasma treatment. (**g, h**), DI water (**g**) and LOR3A (**h**) drops contact angles as a function of plasma parameters. $n = 4$ drops for each sample (except 'DI Water - 2 min, $t = 0'$, 'LOR3A - Pristine' and 'LOR3A - 6 min, $t = 0'$ for which $n = 3$, 5 and 5 drops respectively), value = mean ± S.D. *** $p < 0.001$, two-tailed, unpaired t-test. The results suggest a significant decrease in LOR 3 A contact angle after 6 min plasma treatment, which, however, can only last for less than 30 min. **(i-k)** Bonding input/output (I/O) metal pads to flexible cables. **i**, Schematic of the side view of a brain probe showing that I/O pads are defined on the silica substrate for bonding and connected to interconnects through the smooth edge of the slightly overexposed PFPE-DMA dielectric layer. Flexible cables are bonded through the anisotropic conductive film to I/O pads. **j**, BF microscopic image of a 250-μm-wide I/O pad. Scale bar, 50 μm. **k**, Zoom-in view of the red box highlighted region in (**j**). The focal plane in the images has been adjusted stepwise (indicated by black arrows) to show that the sputtered Al/Au layer deposited on the smooth edge of the PFPE-DMA layer connected with the Cr/Au I/O pads. **l**, Schematic showing that smooth edges of the overexposed PFPE-DMA dielectric layers are necessary for ensuring the metal interconnects from the PFPE-DMA layers can connect to the I/O regions on the silicon oxide substrate. **m**, Pseudo-colored SEM images showing the metal interconnects patterned from the PFPE-DMA layers to the I/O pads on the substrate. Pseudo-colors were used to highlight different metal and PFPE-DMA layers.

https://doi.org/10.1038/s41565-023-01545-6

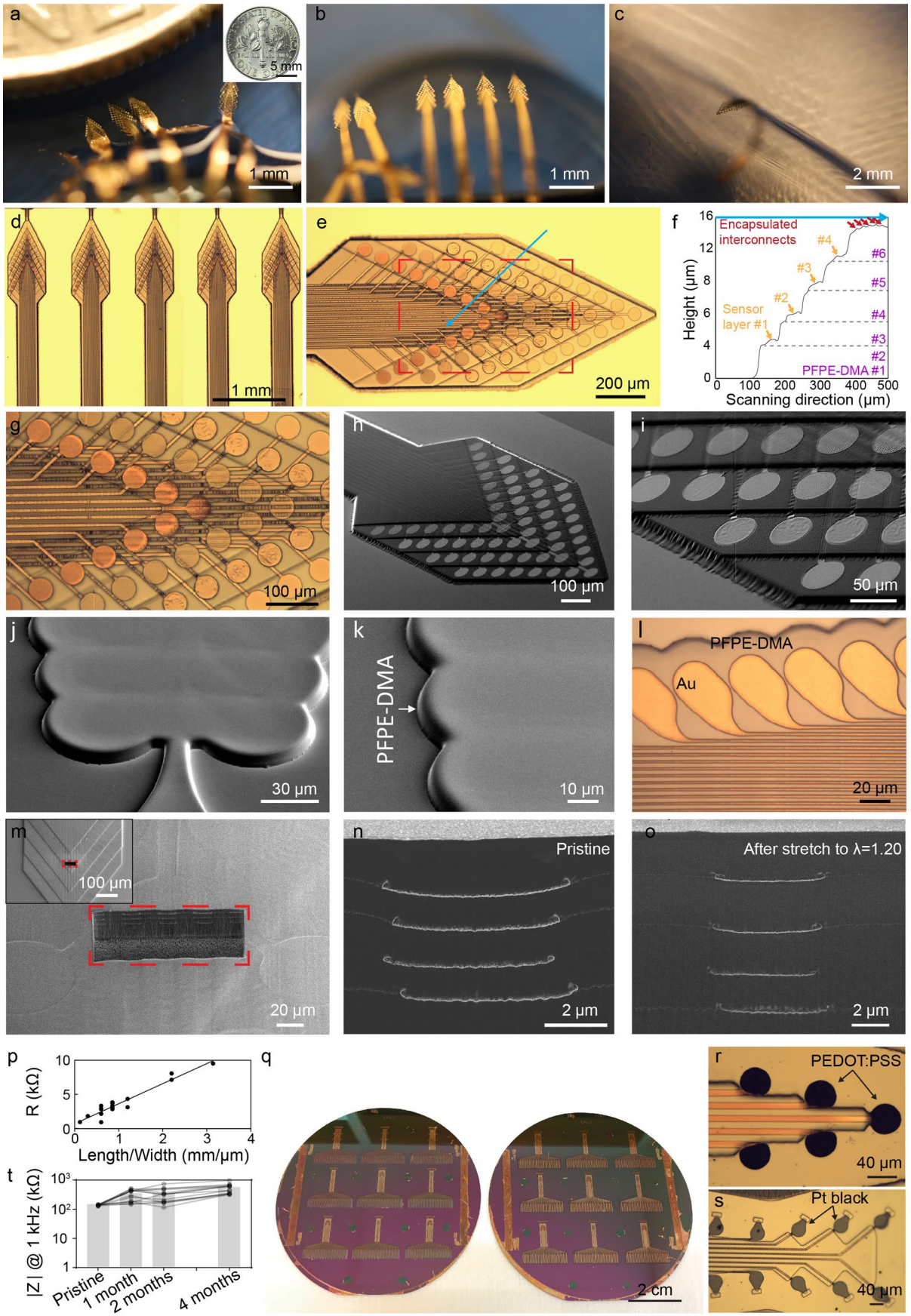

Extended Data Fig. 8 | See next page for caption.

https://doi.org/10.1038/s41565-023-01545-6

Extended Data Fig. 8 | Imaging and characterization of soft neural probes. (**a**-**c**) Array of PFPE-DMA neural probes containing four layers of electrode arrays with 64 channels. The array is positioned next to a ten-cent dime in (**a**), floating on the surface of a water droplet in (**b**), and bent on a thick H-SEBS substrate in (**c**). **d**, Stitched BF optical images showing an array of PFPE-DMA neural probes, each containing four layers of electrode arrays with 64 channels, on a 100-nm-thick nickel layer pattern on a silicon wafer. **e**, Zoom-in BF image showing the sensor region of a representative neural probe. **f**, Height profile along the blue arrow in (**e**) measured by profilometer, showing the smooth PFPE-DMA and metal layers. **g**, Zoom-in view of the region highlighted by the red dashed box in (**e**). (**h, i**), SEM images of the neural probe design seen in (**d, e, g**). **j**-**k**, SEM images of curved edge PFPE-DMA features on a silicon oxide wafer. **l**, Optical images of high-density Au interconnects with a width of 2.4 μm and pitch of 5.0 μm. **m**, FIB combined with SEM showing the cross-section of the red dashed box highlighted region in the inset. (**n, o**) FIB combined with SEM images showing the cross-section before and after stretching the neural probe with four layers of electrode arrays to 20% and releasing them. **p**, Resistance measurement of Al/Au interconnects on PFPE-DMA with different length-to-width ratios. The Al/Au interconnects have a thickness of 40/100 nm. **q**, Wafer-scale fabrication of PFPE-DMA neural probes on two 3-inch silicon oxide wafers. Each wafer contains 9 probes. (**r**, **s**) Electroplating of Pt black on the metal electrodes in PFPE-DMA neural probes. **r**, Sputtered Al/Au electrodes after PEDOT:PSS electrodeposition. **s**, Sputtered Al/Au electrodes after Pt Black electrodeposition by cyclic voltammetry. **t**, Chronic impedance measurements of PFPE-DMA neural probes. Impedance modulus of 40 μm-diameter electrodes with sputtered Pt immediately after device release and after soaking in 1× PBS at 37 °C, $n = 14$ electrodes, value = mean ± S.D.

https://doi.org/10.1038/s41565-023-01545-6

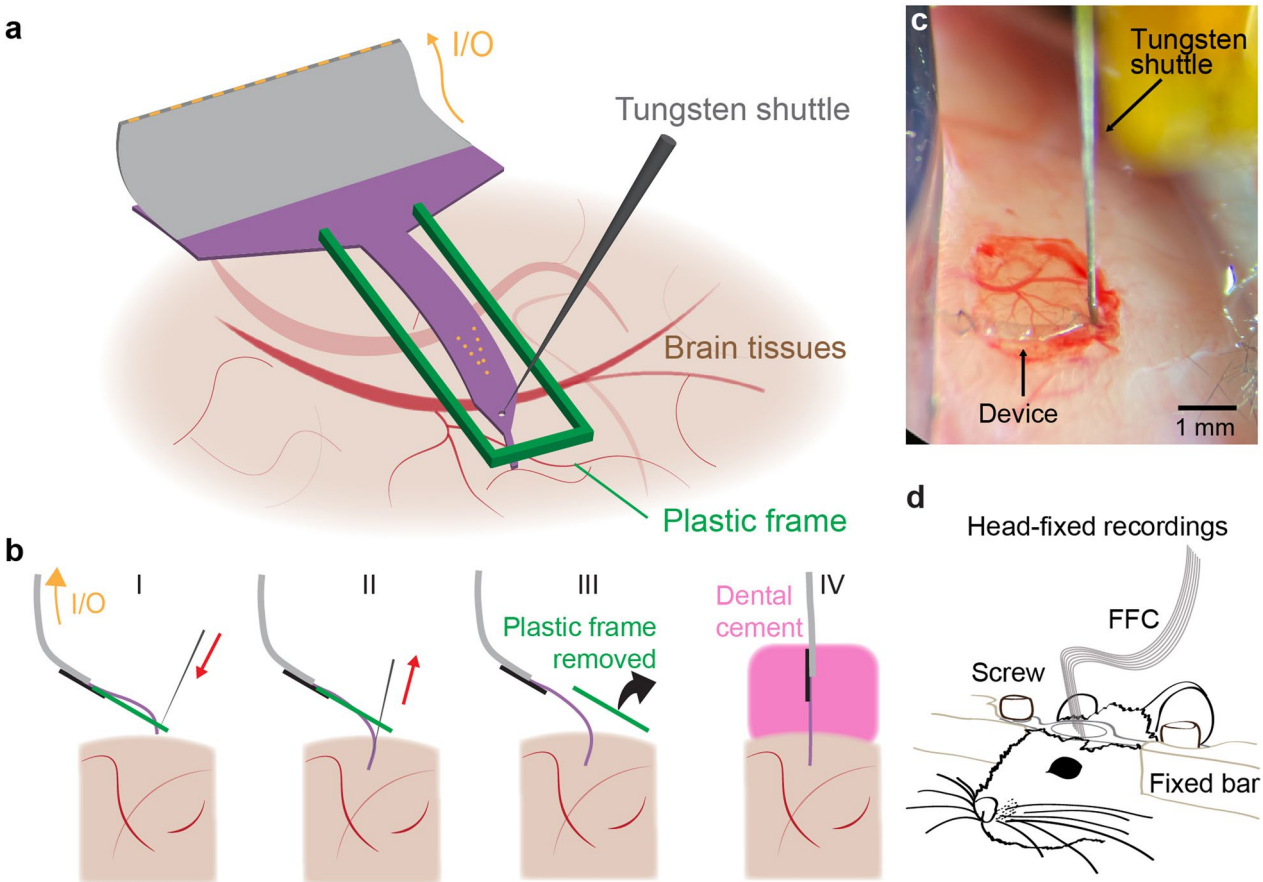

Extended Data Fig. 9 | Implantation of soft neural probes in the mice brain. (**a, b**) Schematics showing the shuttle-driven implantation technique for elastomer-based brain probes. **a**, The brain probe held by a SU-8 plastic frame was transferred to the brain surface. **b**, Schematics showing the implantation steps (side view). (I) After positioning the probe on the brain surface, a tungsten shuttle (core diameter of 70 µm, conically etched at the tip) pokes through a hole at the top of the device and penetrates the brain tissue. (II) Once the desired depth of implantation is reached, the tungsten shuttle is withdrawn from the brain tissue. (III) The SU-8 plastic frame, lying on the surface of the brain, is removed before (IV) sealing the craniotomy area with dental cement. **c**, Shuttle-driven implantation during craniotomy. A soft brain probe is guided inside brain tissues by a tungsten shuttle which pokes through a circular hole at the top of the device. **d**, Schematic of measurement setup for head-fixed mouse.

https://doi.org/10.1038/s41565-023-01545-6

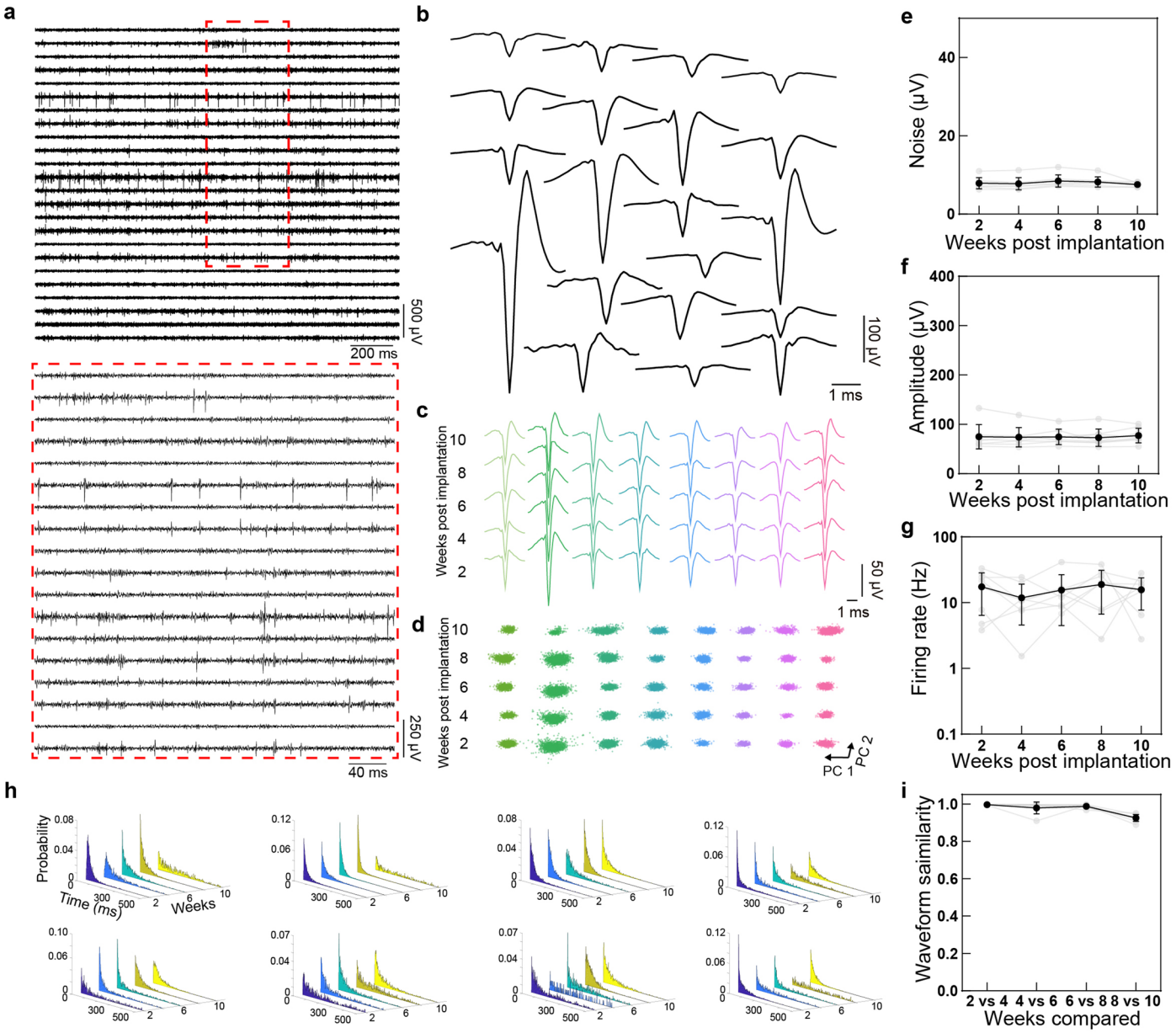

Extended Data Fig. 10 | Long-term stable brain electrophysiology by a 2-μm-thick, single metal-layer soft neural probe. a, (Top) Typical unit activities (300–3,000 Hz bandpass filtered) from a PFPE-DMA soft brain probe at 4-week post-implantation. (Bottom) Unit activities of the dashed red box highlighted region in the top panel. **b**, Average single-unit waveforms detected in (**a**). **c**, Representative average waveforms from 2- to 10-week post-implantation. **d**, Clusters of waveforms detected for each channel in (**c**) as a function of post-implantation weeks in the PCA space. PC1 and PC2 represent the first two axes in the PCA from the clustering algorithm. (**e**-**g**) Noise level per channel (**e**), peak-valley amplitude (**f**), and firing rate (**g**) of the units detected in (**c**) ($n = 8$ units, mean ± S.D.) vs. implantation time. **h**, Biweekly evolution of the ISI distribution for each unit shown in panel (**c**), bin size 2 ms. **i**, Waveform similarity of the units detected in (**c**-**h**) ($n = 8$ units, mean ± S.D.) as a function of post-implantation weeks compared.

nature portfolio

Corresponding author(s): Jia Liu

Last updated by author(s): Oct 6, 2023

Reporting Summary

Nature Portfolio wishes to improve the reproducibility of the work that we publish. This form provides structure for consistency and transparency in reporting. For further information on Nature Portfolio policies, see our Editorial Policies and the Editorial Policy Checklist.

Statistics

For all statistical analyses, confirm that the following items are present in the figure legend, table legend, main text, or Methods section.

n/a	Confirmed	
☐	☒	The exact sample size (*n*) for each experimental group/condition, given as a discrete number and unit of measurement
☐	☒	A statement on whether measurements were taken from distinct samples or whether the same sample was measured repeatedly
☐	☒	The statistical test(s) used AND whether they are one- or two-sided *Only common tests should be described solely by name; describe more complex techniques in the Methods section.*
☒	☐	A description of all covariates tested
☒	☐	A description of any assumptions or corrections, such as tests of normality and adjustment for multiple comparisons
☐	☒	A full description of the statistical parameters including central tendency (e.g. means) or other basic estimates (e.g. regression coefficient) AND variation (e.g. standard deviation) or associated estimates of uncertainty (e.g. confidence intervals)
☐	☒	For null hypothesis testing, the test statistic (e.g. *F*, *t*, *r*) with confidence intervals, effect sizes, degrees of freedom and *P* value noted *Give P values as exact values whenever suitable.*
☒	☐	For Bayesian analysis, information on the choice of priors and Markov chain Monte Carlo settings
☒	☐	For hierarchical and complex designs, identification of the appropriate level for tests and full reporting of outcomes
☒	☐	Estimates of effect sizes (e.g. Cohen's *d*, Pearson's *r*), indicating how they were calculated

Our web collection on statistics for biologists contains articles on many of the points above.

Software and code

Policy information about availability of computer code

Data collection	Blackrock Research Central Software Suite 7.04 was used to acquire electrophysiology data, available at https://blackrockneurotech.com/research/support/software/. Leica Application Suite X software platform 3.5.5 was used to acquire fluorescence images. EC-Lab V11.36 was used with a SP-150e single channel potentiostat from BioLogic for electrochemical impedance spectrums acquisition.
Data analysis	MountainSort 4: https://github.com/flatironinstitute/mountainsort DropSnake: https://bigwww.epfl.ch/demo/dropanalysis/ Deeplabcut: http://www.mackenziemathislab.org/deeplabcut GraphPad Prism 9: https://www.graphpad.com/ Matlab R2022b: https://www.mathworks.com/products/matlab.html Wolfram Mathematica: https://www.wolfram.com/mathematica/ Abaqus 6.12: https://www.3ds.com/products-services/simulia/products/abaqus/

For manuscripts utilizing custom algorithms or software that are central to the research but not yet described in published literature, software must be made available to editors and reviewers. We strongly encourage code deposition in a community repository (e.g. GitHub). See the Nature Portfolio guidelines for submitting code & software for further information.

Data

Policy information about availability of data

All manuscripts must include a data availability statement. This statement should provide the following information, where applicable:

- Accession codes, unique identifiers, or web links for publicly available datasets
- A description of any restrictions on data availability
- For clinical datasets or third party data, please ensure that the statement adheres to our policy

Data and materials availability: All data and materials supporting the findings of this study are available within the paper and its Supplementary Information. The raw datasets generated during the study are provided within the source data. Source data are available for Figs. 1-5, Extended Data Figs. 3-8 and 10. Source data are provided within this paper.

Research involving human participants, their data, or biological material

Policy information about studies with human participants or human data. See also policy information about sex, gender (identity/presentation), and sexual orientation and race, ethnicity and racism.

Reporting on sex and gender	N/A
Reporting on race, ethnicity, or other socially relevant groupings	N/A
Population characteristics	N/A
Recruitment	N/A
Ethics oversight	N/A

Note that full information on the approval of the study protocol must also be provided in the manuscript.

Field-specific reporting

Please select the one below that is the best fit for your research. If you are not sure, read the appropriate sections before making your selection.

☒ Life sciences ☐ Behavioural & social sciences ☐ Ecological, evolutionary & environmental sciences

For a reference copy of the document with all sections, see nature.com/documents/nr-reporting-summary-flat.pdf

Life sciences study design

All studies must disclose on these points even when the disclosure is negative.

Sample size	Sample sizes were estimated based on previous studies. [Yang, X. et al. Bioinspired neuron-like electronics. Nat. Mater. 18, 510-517 (2019).]
Data exclusions	Animals with surgical complications and that displayed health concerns during the post-surgery monitoring period were excluded based on pre-established criteria.
Replication	All the experiments were replicated. The number of repetitions for each experiment has been indicated in the manuscript. Attempts at replication were successful and the conclusion were drawn from the analysis of multiple experiments.
Randomization	Mice were randomized into different groups
Blinding	Investigators were blinded to data collection and analyses of fluorescence images. Blinding was not relevant to this long-term electrophysiological recording because the animals were not divided into control and experimental groups.

Reporting for specific materials, systems and methods

We require information from authors about some types of materials, experimental systems and methods used in many studies. Here, indicate whether each material, system or method listed is relevant to your study. If you are not sure if a list item applies to your research, read the appropriate section before selecting a response.

Materials & experimental systems

n/a	Involved in the study
☐	☒ Antibodies
☒	☐ Eukaryotic cell lines
☒	☐ Palaeontology and archaeology
☐	☒ Animals and other organisms
☒	☐ Clinical data
☒	☐ Dual use research of concern
☒	☐ Plants

Methods

n/a	Involved in the study
☒	☐ ChIP-seq
☒	☐ Flow cytometry
☒	☐ MRI-based neuroimaging

Antibodies

Antibodies used

Primary antibodies:
Chicken anti-glial fibrillary protein GFAP (Abcam, Catalog #ab4674, Lot #GR3281175-3)
Goat anti-ionized calcium binding adaptor molecule 1 (Iba1) (Abcam, Catalog #ab5076, Lot #GR63420-3)
Rabbit anti-neuronal nuclear NeuN (Abcam, Catalog #ab177487, Lot #GR3250076-7)
GFAP (GA5) Mouse mAb (Cell Signaling Technology, #3670)
Iba1/AIF-1 (E4O4W) XP® Rabbit mAb (Cell Signaling Technology, #17198)
All primary antibodies were diluted 1:100-1:200

Secondary antibodies:
Alexa Fluor 647 donkey anti-chicken (Jackson Immunoresearch, Catalog #a703605133, Lot #GR144948)
Alexa Fluor 647 goat anti-mouse (Invitrogen, Catalog#A21236)
Alexa Fluor 594 donkey anti-goat (Invitrogen,Catalog #A32758, Lot #TI271731)
Alexa Fluor 555 goat anti-rabbit (Invitrogen, Catalog#A21429)
Alexa Fluor 488 donkey anti-rabbit (Invitrogen,Catalog #A21206, Lot #2045215)
All secondary antibodies were diluted 1:500

Validation

Validation statement on the manufacturer's website and citations such as https://www.abcam.com/gfap-antibody-ab4674.html, https://www.abcam.com/neun-antibody-epr12763-neuronal-marker-ab177487.html, https://www.citeab.com/antibodies/2401269-a-21236-goat-anti-mouse-igg-h-l-highly-cross-adsor.
Yang, X. et al. Bioinspired neuron-like electronics. Nat. Mater. 18, 510-517 (2019).

Animals and other research organisms

Policy information about studies involving animals; ARRIVE guidelines recommended for reporting animal research, and Sex and Gender in Research

Laboratory animals	C57BJ/6 mice (25–35 g; 6–8 weeks of age). Mice were housed at a temperature is 22 ± 1 degree Celsius and humidity is 30-70%.
Wild animals	The study did not involve wild animals.
Reporting on sex	Sex was not consider in this work
Field-collected samples	The study did not involve samples collected from the field.
Ethics oversight	All procedures were approved by the Animal Care and Use Committee of Harvard University under protocols 19-03-348 and 20-05-368 .

Note that full information on the approval of the study protocol must also be provided in the manuscript.